To Mum and Dad,
the hardest-working people I know,
and to my Brother,
in whose footsteps I follow

Rafael Alvarado Trujillo
New Mexico Institute of Mining and Technology
December, 2004

SEISMIC NOISE CHARACTERIZATION AT THE MAGDALENA RIDGE OBSERVATORY INTERFEROMETER SITE

by

Rafael Alvarado Trujillo

Submitted in Partial Fulfillment

of the Requirements for the Degree of

Master of Science in Geophysics (Solid Earth)

New Mexico Institute of Mining and Technology

Socorro, New Mexico

December, 2004

ABSTRACT

We performed a seismic site characterization in central New Mexico for the ∼350-m-baseline Magdalena Ridge Observatory (MRO) astronomical interferometer, which will operate at wavelengths between 600 nm and 2400 nm. The operation of an interferometer requires that optical path lengths be stable to within considerably less than one wavelength over the measurement timescale. The study analyzed 1-hour absolute and differential background noise windows at element locations between February and October of 2003. Data were acquired with IRIS PASSCAL stations consisting of four 3-component Streckeisen sensors in shallow vaults and Quanterra Q330 digitizers with both real-time 802.11-telemetry and on-site Baler14 recorders. Sensors were deployed at the ends of each of the three interferometer arms, and at the center of the array. The analysis focused on seismic noise during local night-time hours. Although much of the emphasis of this study is on maximum noise levels at MRO, it is clear from the power spectral density plots of the median and lowest noise periods observed, as well as from the ground displacements recorded during these periods, that night-time noise levels at the site typically reside in the lower half of the Global Seismic Network low noise model and that they are favorable for the operation of the interferometer. With the ex-

ception of noise inside the microseismic band ($\sim$ 0.1 to 0.7 Hz), background noise is generally incoherent at both longer and shorter periods. Differential noise in the short-period band ($<$ 1 s) is of particular interest, as it poses the greatest challenges for active optical systems. In general, hourly differential ground displacements are well below the 25-nm upper limit for acceptable motion during the noisiest nights of the year (9 to 10 nm, on average), even during periods of high wind. We have analyzed the typical duration and recurrence of local, regional, and long-distance earthquakes and estimated the total operational downtime of the interferometer due to these naturally-occurring transient phenomena to be only 21 hours per year. While we have analyzed the noise produced by a 150-kW generator run by a V12 Detroit Diesel engine $\sim$600 m from the center of the seismic array and deemed its effect to be negligible for interferometry, we have found traffic to be the artificial transient phenomenon most likely to produce average differential ground displacements ($>$ 1 Hz) larger than 25 nm and thus induce loss of interferometer coherence. We conclude that the MRO site is moderate in seismic background noise for a continental interior site and is overall suitable for building and operating the proposed interferometer, should the recommendations given herein be appropriately considered in the effort to circumvent the issues above mentioned.

ACKNOWLEDGMENT

I would like to first thank my advisor Rick Aster for his outstanding professional guidance and for believing that I would make a good Master's candidate in the first place, as well as Harold Tobin and Brian Borchers, also in my advisory committee, for their valuable contributions to this thesis. The thesis contents are essentially modeled after the suggestions of Chris Haniff and Dave Buscher, who also provided valuable insight into the principles of astronomical interferometry and constructive criticism during the writing stages. Glen Gettemy's help in troubleshooting (Antelope 4.5) and in handling the massive amounts of data was invaluable throughout this project. Brady Romberg wrote the most elaborate of the several MATLAB scripts used for the data processing in this study. Brady's summer internship here at Tech was possible thanks to the IRIS Education and Outreach Internship Program. Dan Klinglesmith was fundamental in the installation of the seismic stations and provided useful suggestions in our several meetings with the MRO group. Craig Wallace was as fundamental as Dan in station installation and it was thanks to him that I did not have to dig a single meter-deep pit at 3,000 meters above sea level. The IRIS PASSCAL Instrument Center at New Mexico Tech provided the equipment and logistic support for field operations and data flow: from Tom Jackson I learned how to install an STS-2 seismometer; Tim Parker taught me everything I needed to know about the Q330 digitizer and the Baler recorder; Bruce Beaudoin introduced me to the essentials of the Antelope data-managing

software; Eliana Gutierrez and Mary Templeton kindly assisted me at several points during the data acquisition and processing stages. Many thanks to all other people who somehow contributed to the completion of this project: professors John Schlue and Allan Sanford with their knowledge of Socorro seismicity; professor Sue Bilek with her knowledge of regional seismicity; professors Charles Chapin and Richard Chamberlin with their knowledge of South Baldy geology; Pierce Howell with his magnificent MRO maps (thanks to Rob Selina for making them accessible to me in digital form); Ifan Payne with a copy of the AMEC geotechnical report; and professor Bill Winn at Langmuir Lab with the Detroit Diesel engine investigated herein. I would also like to thank my other fellow Geophysics graduate students for their daily encouragement and peculiar sense of humor; Dave Wilson was particularly helpful whenever MATLAB did not behave, and Matt Richmond was extremely helpful whenever anything computer-related did not behave. This project was funded by Los Alamos National Laboratory, but it would have been impossible to start in the first place without the moral and financial support of my family in Peru.

This thesis was typeset with LaTeX[1] by the author.

[1] LaTeX document preparation system was developed by Leslie Lamport as a special version of Donald Knuth's TeX program for computer typesetting. TeX is a trademark of the American Mathematical Society. The LaTeX macro package for the New Mexico Institute of Mining and Technology thesis format was adapted from Gerald Arnold's modification of the LaTeX macro package for The University of Texas at Austin by Khe-Sing The.

TABLE OF CONTENTS

LIST OF TABLES

LIST OF FIGURES

This thesis is accepted on behalf of the faculty of the Institute by the following committee:

Richard C. Aster, Advisor

Rafael Alvarado Trujillo Date

CHAPTER 1

INTRODUCTION

1.1 What is seismic background noise?

Everywhere on the planet, even in stable, mid-continental locations far away from the boundaries of tectonic plates and from cities bustling with activity, the ground on which we stand vibrates weakly but continuously. Despite their small amplitudes, these continuous movements of the Earth's crust have been recorded since the early days of modern seismometry and, because they can overlap with or even swamp the more useful signals produced by transient phenomena (*e.g.*, earthquakes), they are collectively referred to as seismic background noise. This omnipresent seismic background noise is caused by a variety of agents that may be naturally-occurring (*e.g.*, oceans and wind) as well as man-made (*e.g.*, traffic and industrial activity), all of which are capable of coupling to the ground to generate seismic waves. For example, wave activity near coastlines and deep ocean waves exciting the underlying oceanic crust are responsible for the most prominent noise peak observed at both ocean-bottom sites and continental sites worldwide, the so-called oceanic microseism near 7 s ($\sim$0.14 Hz) in Figure 1.1. Similarly, wind gusts coupling to the ground through the roots of swaying trees are responsible for some of the high-frequency noise peaks observed at continental sites during windy periods. By shaking the ground on which scientific instruments are set, seismic background noise of a specific strength and in particular frequency bands might pose a problem for

high-precision measurements, such as those involved in astronomical interferometry.

1.2 Noise spectra

We can analyze the frequency content of a *transient* or finite-duration signal $f(t)$ generated by a seismic source, such as an earthquake or an explosion, by looking at the signal's Fourier transform $F(\omega)$, where t is the time and ω the angular frequency (*e.g.*, Aki and Richards, 2002). To analyze the frequency composition of a *continuous* noise signal we look at its power spectral density $PSD(\omega)$,

$$PSD(\omega) = \int_{-\infty}^{+\infty} P(\tau) e^{i\omega t}\, d\tau. \tag{1.1}$$

Here $P(\tau)$ is the autocorrelation function, defined as

$$P(\tau) = \langle f(\tau) f(t+\tau) \rangle, \tag{1.2}$$

where the brackets indicate averaging over t.

1.3 Global high and low noise models

Peterson (1993) has constructed global high and low seismic background noise models (Fig. 1.1) that are composites of PSD extrema, based on a comprehensive noise survey of stations around the world. The composites, referred to as the high noise model (HNM) and low noise model (LNM), were obtained by overlaying the PSDs of representative noisy and quiet periods at individual stations, picking the highest- and lowest-noise points at each frequency of the overlay while disregarding any narrow peaks or valleys in the spectrum of particular stations, and fitting high- and low-noise envelopes in

the overlay with straight-line segments. Earthquake signals and other transient phenomena were avoided in constructing the models. Because the noise data used to compute individual PSDs were recorded almost exclusively by Global Seismic Network (GSN) stations with instruments sensitive to different frequency bands, and hosted in different vault types (*e.g.*, surface, subsurface, and borehole) in various geologic conditions (from granitic and basaltic to alluvial and icy) over a period of twenty years, the high and low noise models can be expected to characterize fairly reasonably high and low background noise periods around the world. However, no particular location on Earth is likely to be as noisy or as quiet as the models through the entire frequency band displayed; the noise PSD of a typical station (Fig. 1.1) will lie somewhere between the HNM and LNM curves, and will exhibit two distinct peaks at about 7 s (∼0.14 Hz) and 14 s (∼0.07 Hz), respectively, both due to ocean activity.

1.4 Interferometry basics

An astronomical interferometer is an array of telescopes whose individual light beams are combined into a single beam to provide the resolving power of a single, much larger and thus much more expensive telescope having approximately the same physical dimensions as the array. However, the benefits of such an array do not come without a cost: Fast fluctuations in the interferometer optical paths, such as those caused by atmospheric fluctuations and seismic background noise, have been known to cause problems for astronomical interferometry (*e.g.*, Buscher *et al.*, 1995).

The superposition of light beams from individual telescopes produces an interference pattern with alternating bright and dark regions resulting, re-

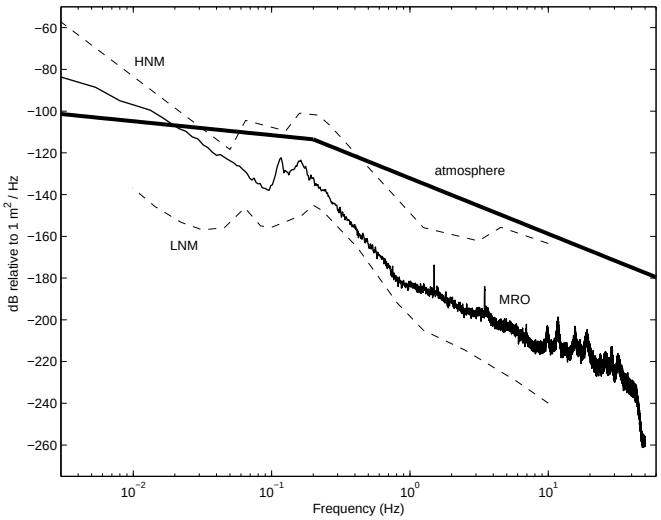

Figure 1.1: Comparative noise displacement spectra: global high and low noise models (dashed curves) and PSD of a typical station lying within the two global noise curves. The typical PSD corresponds to a median-noise night-time hour of data recorded by the east-west component of a seismic station at the Magdalena Ridge Observatory site in the middle of the spring. For comparison with the high noise model, the PSD of the atmosphere (solid curve), is also shown. It corresponds to Kolmogorov's model (Buscher *et al.*, 1995), which assumes a single turbulent layer moving perpendicular to the interferometer baseline at 31.5 m/s. The scaling parameter r_0 for this theoretical model is 1.2 m, and the seeing at 500 nm is $\sim$0.086 arcseconds. At frequencies greater than about 1 Hz, the Kolmogorov model is representative of the atmospheric fluctuations typically observed at a good site for astronomical seeing. It is a rule of thumb in astronomical interferometry that, at a particular site, seismic background noise will not be a problem as long as it is well below the noise level produced by atmospheric fluctuations at the site (*e.g.*, by a factor of 5).

spectively, from the constructive and destructive interference of the optical wave trains. It is from this fringe pattern that astronomers gather the information to build the image of the celestial object being observed. For the fringe pattern to provide useful information, it must remain stationary long enough for the fringe contrast to be accurately measured (that is, $(I_{max} - I_{min})/(I_{max} + I_{min})$, where I_{max} and I_{min} are the maximum and minimum fringe intensities, respectively); losses in fringe contrast due to motion of the fringes during their measurement will compromise the performance of the interferometer. Seismic activity and atmospheric turbulence can lead to fluctuations in the *optical path lengths* or OPLs (that is, the distances covered by the light beams from each telescopes to the point of interference), thereby producing non-stationary fringe patterns.

Evidently, seismic activity and atmospheric turbulence are inescapable sources of OPL-fluctuation for ground-based interferometers. Fortunately, there is a safe range within which OPLs may fluctuate at any time during the fringe-contrast measurement without causing relevant loss of coherence in the fringe pattern: optical path fluctuations must be shorter than a small fraction of the characteristic wavelength of the array, typically taken to be close to the minimum wavelength sensed by the telescopes that make it up. Moreover, modern technology allows interferometers to handle fluctuations of any reasonable magnitude as long as these fluctuations are slow enough, typically below 1 Hz: active optical systems compensate for these optical path fluctuations using computer-adjusted delay lines which make the fringe pattern stationary for all practical purposes (*e.g.*, Haniff and Buscher, 2003). However, rapid fluctuations above 1 Hz cannot be corrected in this manner and therefore pose a potentianlly serious problem for interferometry.

1.5 Purpose of this study

The purpose of this study is to quantitatively evaluate ground motion at the site of the future Magdalena Ridge Observatory (MRO) interferometer and determine, in particular, whether seismic activity faster than 1 Hz results in ground displacement (and, consequently, optical path fluctuations) greater than a twentieth of the characteristic wavelength of the interferometer. We will also address what causes such displacement, how often it occurs (if transient rather than continuous in nature), and what can be done to isolate the astronomical instruments from it.

Because astronomical observations with the MRO interferometer will utilize infrared wavelengths as large as 2400 nm and optical wavelengths as short as 600 nm, the characteristic wavelength (λ_o) of the interferometer is taken to be close to the lower bound of this range, namely 500 nm. When taken to be $\lambda_o/20$, the upper bound for acceptable ground displacement, that is, displacement that will not result in loss of interferometer coherence, is 25 nm. By choosing the characteristic wavelength of the interferometer to be approximately the smallest wavelength it is sensitive to, rather than the largest or any wavelength in between, we ensure that the upper bound for acceptable ground displacement indeed represents an upper bound for all wavelengths the interferometer is sensitive to. Although in this study we will be frequently comparing ground displacements observed at MRO against the 25-nm mark, it is important to realize that the 25-nm upper bound is not set in stone but is only a rough reference point which can be thought of as a typical or mean upper bound for acceptable ground displacement and which may be either relaxed or

tightened. In other words, depending on the specific observation to be made with the interferometer, the upper bound of acceptable displacement could be an either larger or smaller fraction than a twentieth of the characteristic wavelength. Giving the upper bound a fixed number in this study rather than assigning it a symbol (*e.g.*, U), is of much help in the forthcoming analysis, as it provides us with a standard"ceiling" with which to compare the displacements observed at all seismic stations used in this investigation.

As a matter of fact, the operation of an interferometer requires that the fringes not move by more than $\sim \lambda_o/30$, which results in a $\sim 5\%$ loss in fringe contrast. In most interferometers, a total of $\sim 10\%$ loss is allowed, some of which results from the fact that the movable optics in the interferometer are not moved exactly as they should and hence shake. Assuming that ground fluctuations and imperfections in the design of the active optics are the only sources of undesirable fringe motion and thus undesirable loss of fringe contrast, the maximum allowable ground displacement is directly dependent upon the maximum fringe displacement that the imperfect active optics system causes. If, with hindsight, we assume that poor design of the active optics and ground fluctuations each account for 5% of the 10% maximum allowable loss of fringe contrast (that is, each causes fringe motion of $\sim \lambda_o/30$), then it would be better to take $\lambda_o/30$ as the upper limit of acceptable ground displacement. This is somewhat more stringent that the $\lambda_o/20$ (i.e., 25 nm) used herein.

Moreover, because a crucial requirement of interferometry is that the OPLs from all telescopes be matched accurately to obtain a stationary and measurable fringe pattern, the *relative* ground displacements between pairs of

telescope sites will be of most interest and it will be these differential ground motions which will be required not to exceed ∼25 nm. Nevertheless, measurements of absolute ground displacements at any one telescope site are also important because they help to establish upper bounds for the crucial differential ground displacements, as will be discussed later. It is now understandable why, unlike multiple-telescope observatories, single-telescope observatories do not require a detailed seismic characterization study: although their operation also requires the combination of light beams, in single telescopes all of the optics are usually on the same structure, so if the whole structure shakes only very small optical path fluctuations result; moreover, large fluctuations in OPLs are usually not detrimental to single-telescope astronomy, although this depends on the mode in which the telescope is operated. In fact, MRO will also feature a telescope that will be independent of and larger in diameter than the telescopes making up the interferometer, and for which ground displacements of the amplitudes and frequencies we consider here will be of much less concern.

It is important to keep in mind that this study is about displacement due to ground motion only; it does not address how the interferometer hardware (*e.g.*, mirror mounts) will actually respond to the ground motion. If the interferometer hardware has resonances at frequencies above 1 Hz, then the actual displacement of the optics will have an amplitude larger than that of the ground motion by itself. Although what is needed to predict the actual displacement of the optics is a full finite element model of the mechanical components of the interferometer (which is unavailable because the interferometer itself does not exist yet), it is expected that the interferometer optics will be designed so that they do not have strong resonances at high frequencies, but

even if they do there will certainly be an appropriate measure of damping in the design to limit the transfer of ground motion into the optics.

CHAPTER 2

SITE LOCATION

Magdalena Ridge, future host of the MRO interferometer and deployment site for the seismic array used in this study, is a narrow line of high ground on the north-trending Magdalena Mountains, a complex set of uplifted and tilted fault blocks roughly 32 km long by 11 km wide altogether, standing on the west side of the Rio Grande rift valley in Socorro County, central New Mexico (*e.g.*, Bowring, 1980). The ridge, approximately 16 km south of the town of Magdalena (Fig. 2.1) and accessible through U.S. Forest Service Road 235 from U.S. Highway 60, bridges the summit of South Baldy Peak, which is the highest peak in the Magdalena Mountains (3287 m), and the peak hosting the Langmuir Laboratory for Atmospheric Research (3240 m) to the south.

Structurally, Magdalena Ridge is the crest of a single fault block dividing Magdalena cauldron, to the west, from Sawmill Canyon cauldron, to the east. The block has a crude dumbbell shape and stands as a topographic high (Fig. 2.2) because it failed to subside as much as the two adjacent cauldrons following their respective eruptive episodes. Magdalena Ridge is characterized by closely-spaced, north-trending, nearly-vertical normal faults that are believed to belong to the same group of faults along which the Magdalena Mountains were uplifted during the late Miocene and Pliocene, 7 to 4 Ma ago, rather than to the group of older, deeper faults triggered by the beginning of the extensional

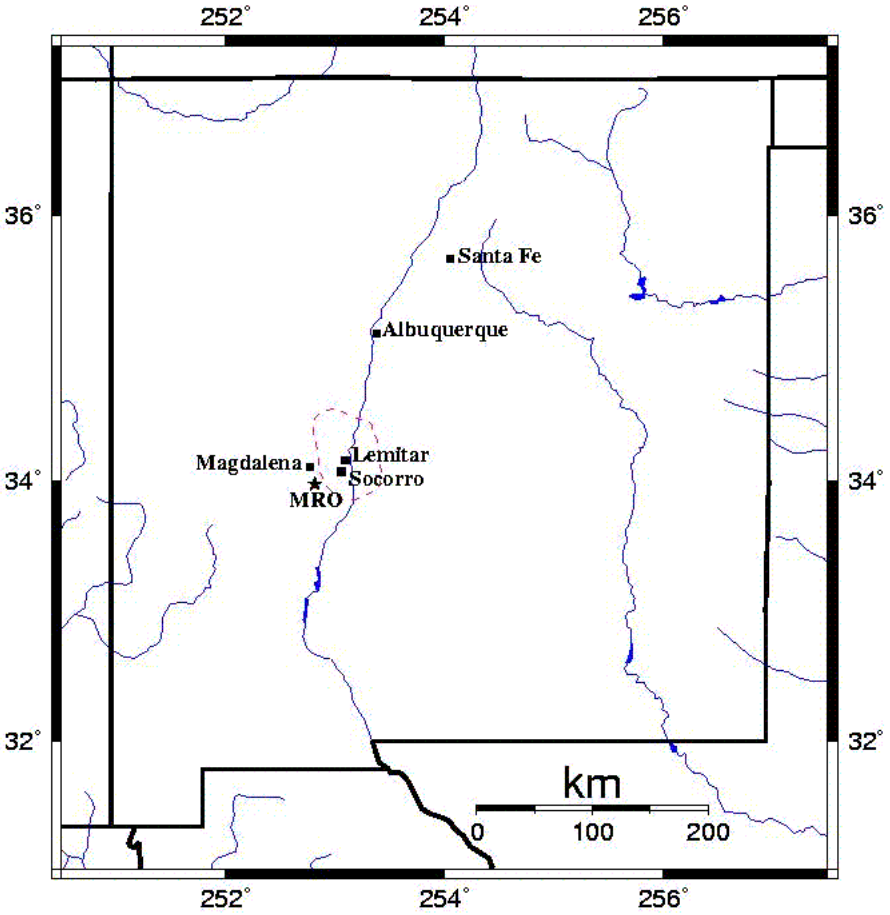

Figure 2.1: Map of New Mexico showing the location of the MRO site (north is up). The dashed line encloses the mid-crustal Socorro magma body (subsection 5.2.1), thought to be the source of small-magnitude but relatively frequent local earthquake activity. Note that, conveniently enough, the MRO site is just outside the Socorro magma body. Curved solid lines are major rivers and relevant cities are indicated by a solid square. The river running through Albuquerque and Socorro is the Rio Grande and sits roughly along the middle of the north-trending Rio Grande rift, which has been opening for the last 30 Ma or so.

Figure 2.2: Aerial view of the future site of the MRO interferometer, in the neighborhood of South Baldy Peak (near top left corner) in the Magdalena Mountains, central New Mexico, January 2003. (Photo courtesy of Dan Klinglesmith.)

regime of the Rio Grande rift, about 32 to 28 Ma ago (Bowring, 1980).

The impact of local, regional, and long-distance earthquake activity on the MRO site is elaborated upon to some detail in Chapter 5.

The Y-shaped, four-element seismic array used in this study was deployed on the relatively flat area of Magdalena Ridge on which the three-arm interferometer will stand (Fig. 2.3). A seismic station was installed at the end of each of the three arms, while the fourth station was installed at the intersection of the arms, approximately 1.4 km south of the summit of South Baldy. Although the terrain to both east and west of the deployment area slopes downward abruptly, the elevation of the deployment area itself does not stray by more than a few meters from its approximately 3200-m average.

The shallow geology of the deployment area is dominated by laharic breccia and purple rhyolite (Stacy, 1968), the rocky erosional debris of which are extensively found on the surface. Derived from the Datil-Mogollon vol-

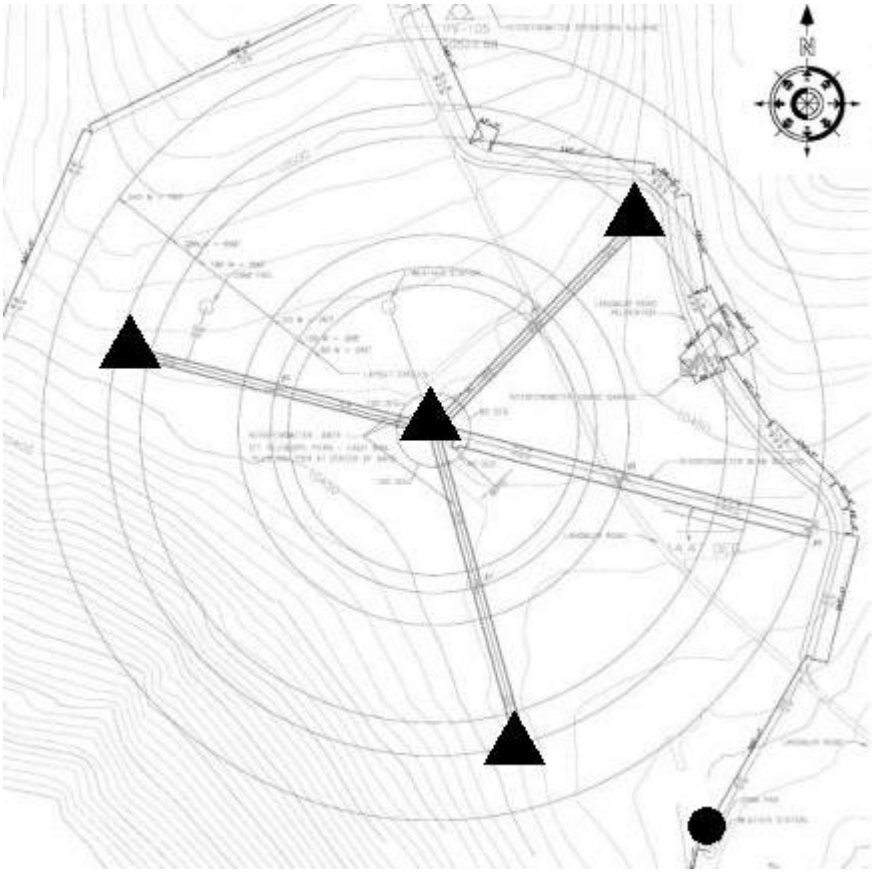

Figure 2.3: Blueprint showing the main features of the MRO interferometer design, as well as the local topography. For a horizontal scale, note that each of the three interferometer arms is 200 m long. The locations of the four seismic stations used in this study are indicated by the black triangles. The black circle indicates the location of weather station MROI (section 4.4), roughly 350 m from the station at the center of the seismic array. Weather station MROST is roughly 900 m north of the center of the array. The center of the array itself is $\sim$1.4 km south of the summit of South Baldy. The power generator used in this study (subsection 5.2.5) is approximately 600 m east-southeast of the center of the array. (Basemap by Pierce Howell, courtesy of Rob Selina.)

canic province, these rocks were originally mapped by Weber (1963) as part of the Datil Formation, deposited approximately 29 to 38 Ma ago during the Oligocene and Upper Eocene (Tertiary), but were later recognized to be part of the Popotosa Formation of more recent deposition (Chapin and Seager, 1975). According to Stacy's mapping of the area, based on the analysis of neighboring outcrops, the purple rhyolite is the most extensive unit on Magdalena Ridge, with a thickness of approximately 850 to 1300 ft. The rhyolite is overlain uncomformably by the South Baldy andesite on the northern end of the ridge and by a thin (50- to 370-ft-thick) unit of laharic breccia on the western half of the ridge, where most of the interferometer will sit. Bowring (1980) later expanded on the work by Stacy and re-classified the thick, extensive purple rhyolite unit underlying the laharic breccia into several thinner units: the upper and lower tuff of Lemitar Mountains, and the (informally named) unit of Sixmile Canyon.

The results of the geotechnical study by AMEC Earth & Environmental at the future site of the interferometer during September and October 2003, which included the drilling of a 35-ft-deep borehole near the deployment site of each of the seismic stations, suggest that neither the unit of purple rhyolite nor the unit of laharic breccia (Fig. 2.4) provide competent bedrock within the upper 80 ft of the site's profile (AMEC, 2004). In fact, while agreeing with Stacy that the shallow subsurface of the site is dominated by a unit of breccia (occasionally interbedded with thin units of clay or sand, adds the geotechnical report), the geotechnical report further shows that the breccia consists of gravels, cobbles and boulders between 2 and 10 ft in diameter (Fig. 2.7), most of them angular fragments of rhyolite and other extrusive volcanic materials, in a matrix of sand and clay. Stacy reported that the matrix makes up, on average,

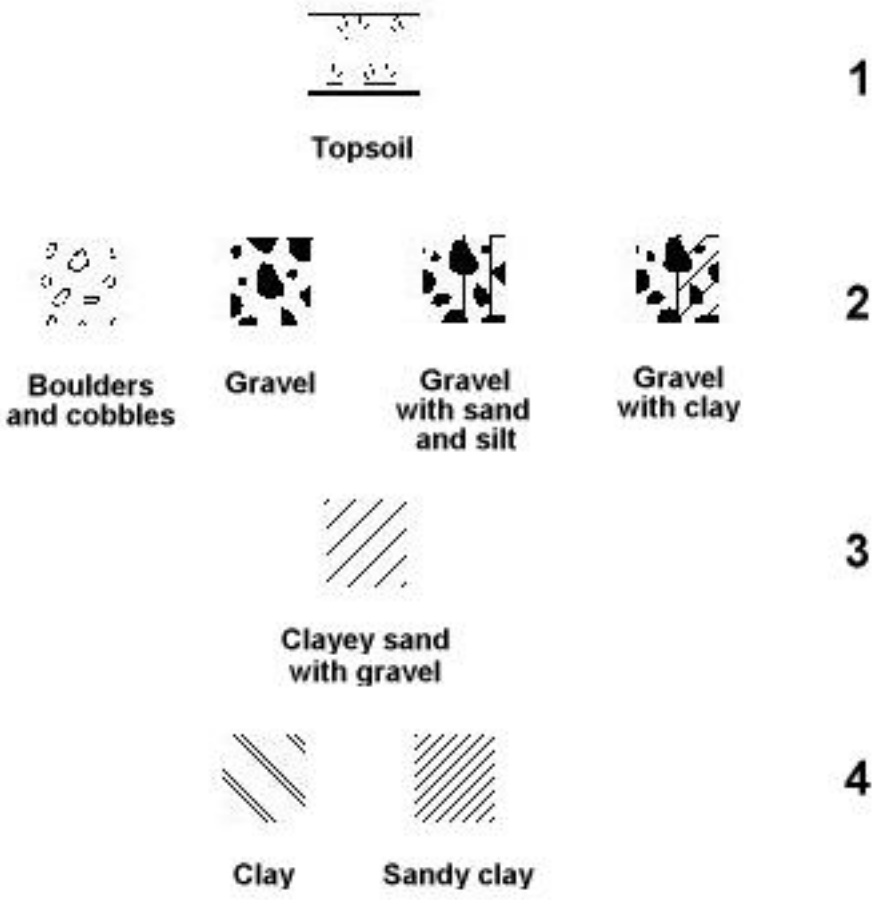

Figure 2.4: Composition of the unit of laharic breccia underlying the MRO interferometer site. Under a foot-thick layer of topsoil (row 1), the breccia consists of units of gravel (row 2), sands (row 3) and clays (row 4), organized in the shallow subsurface as shown in Fig. 2.5 and Fig. 2.6. Soils progressively decrease in coarseness from row 2 to row 4: clays are the finest-grained soils of the three groups. None of these units qualifies as competent bedrock. (After AMEC, 2004.)

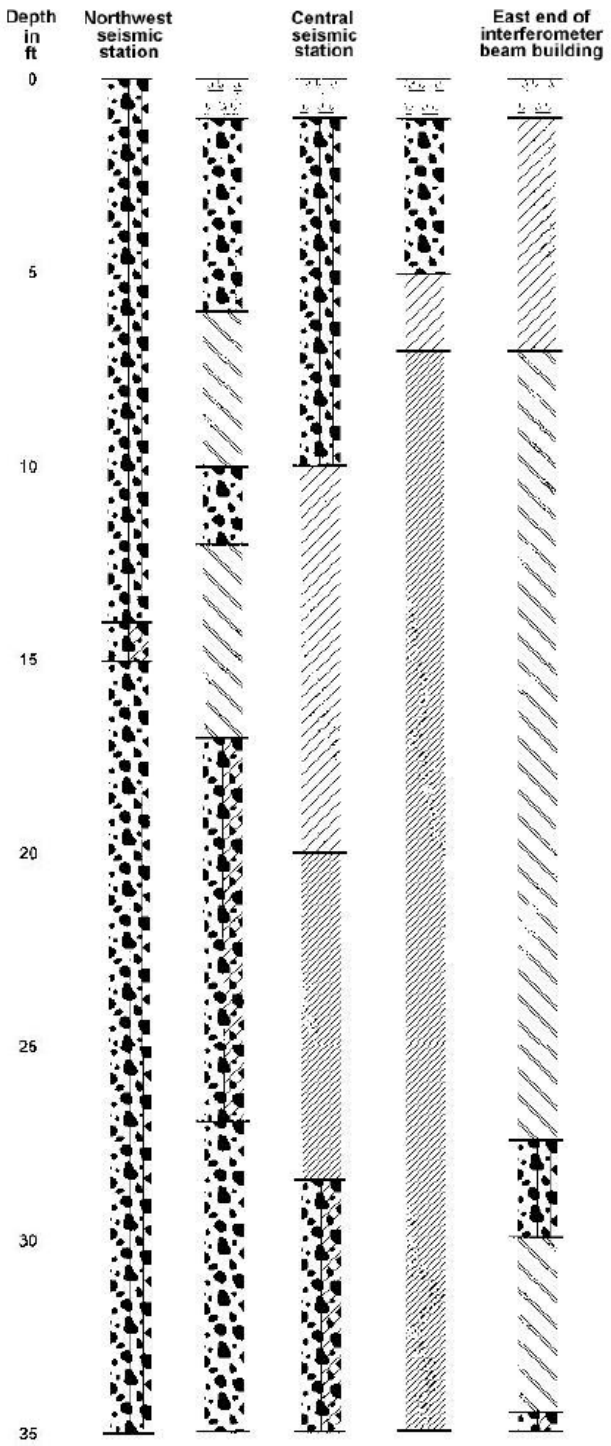

Figure 2.5: Stratigraphic cross-section running roughly west-to-east across the MRO interferometer site, to a depth of 35 ft, based on equally-spaced boreholes. The interferometer beam building is the ∼200-m-long "fourth arm" of the Y-shaped array in Fig. 2.3. See Fig. 2.4 for a legend. (After AMEC, 2004.)

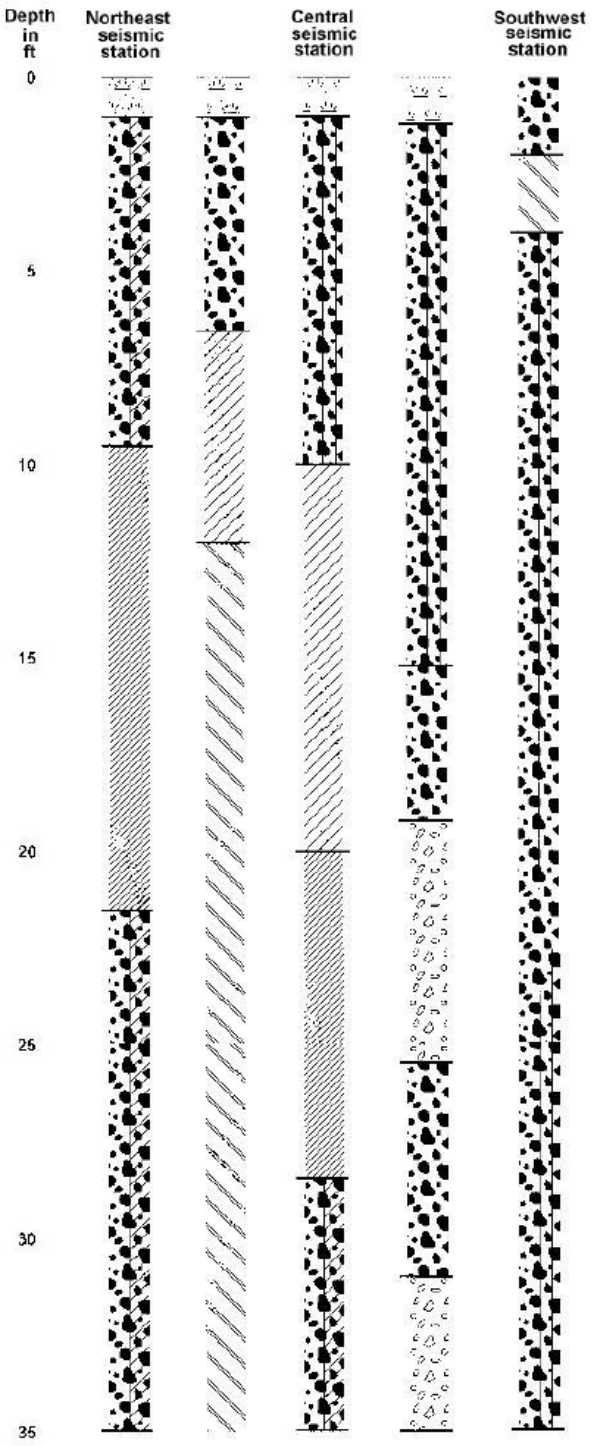

Figure 2.6: Stratigraphic cross-section running roughly north-to-south across the MRO interferometer site, to a depth of 35 ft, based on equally-spaced boreholes. See Fig. 2.4 for a legend; as in the previous cross-section, note the lack of competent bedrock. (After AMEC, 2004.)

half the volume of the breccia in this area and that clay makes up as much as 30% of the matrix. Also agreeing with Stacy that clay is the relatively weak binding agent in the breccia, the geotechnical report suggests that the breccia unit may be considered a "rock and soil pile with upper layers forming a loose blanket of smaller particles that [were] weathered or eroded from the surface."

At three boreholes sites (close to the three westernmost seismic stations in Fig. 2.3), drilling did not go deep enough into the layer of breccia to penetrate the upper tuff of Lemitar Mountains described by Bowring. Although from the geologic maps by Stacy and Bowring it seems that the remaining seismic station was sitting on the upper member tuff of Lemitar Mountains rather than on the unit of laharic breccia, the AMEC drilling logs at this particular site are overall no different from those at the other three sites (Fig. 2.5 and Fig. 2.6). We thus infer that the shallow geology down to a depth of at least 35 ft is essentially the same at all seismic station sites and thus should not be responsible for any differences in seismic response from station to station.

Figure 2.7: Rhyolite boulder found while digging the pit in which CNTR was to be installed. A glove sitting on the boulder serves as a scale. (Photo courtesy of Day Frostenson.)

CHAPTER 3

DATA ACQUISITION

All of the seismic noise data used in this study were acquired with four seismic stations, the components of which were borrowed from the Socorro-based Program for Array Seismic Studies of the Continental Lithosphere (PASSCAL) Instrument Center, a facility of the Incorporated Research Institutions for Seismology (IRIS).[1] Stations were installed between November 2002 and April 2003 and data was recorded between February and October 2003. Each station consisted of a three-component broadband Streckeisen STS-2 sensor in a shallow vault and a Quanterra Q330 acquisition system with both real-time 802.11-telemetry and an on-site Baler14 recording continuously at 100 samples per second (SPS). Sensors were deployed at the end of each of the three interferometer arms, and at the center of the array (Fig. 2.3).

In what follows we limit ourselves to a brief discussion of each of the most crucial features in the STS-2/Q330 digital recording systems used in this study (frequency response, dynamic range, etc.). A more thorough treatment of the theory and usage of seismometers in general can be found in the article by E. Wielandt (2002), who in the early 1980s pioneered the development of high-performance broadband seismometers with G. Streckeisen. Detailed guidelines for installing the STS-2 and for broadband vault construction are available in the PASSCAL Field Manual (IRIS, 1994). Another authority on the

installation of broadband seismic instrumentation is the Berkeley Seismological Laboratory (Uhrhammer and Karavas, 1997), active in the field since 1986.

3.1 Data acquisition instruments

The STS-2, manufactured by *G. Streckeisen AG*, is an electronic, three-component seismometer with a free period of 120 s, which measures ground velocity in a passband with corners at 120 s and at ∼50 Hz. The unusually broad frequency range of recording of this sensor, from which it inherits its "broadband" label, is a direct consequence of the unusually long natural period (120 s) of each of its three 300-g pendulum masses (Fig. 3.1). Although increasing the free period of a mechanical pendulum seismometer leads to instability and nonlinearity, an electronic seismometer with a force-feedback mechanism (*e.g.*, Aki and Richards, 2002) provides a long free period without inducing either of these two undesired effects.

The performance of a seismometer can be described in the frequency domain by its *frequency response*. Because seismometers are designed as linear, time-invariant systems (*e.g.*, Bracewell, 1978), their output signal $\xi(t)$ is related to an input ground motion $u(t)$ simply by $\xi(\omega) = f(\omega)u(\omega)$, where $\xi(\omega)$ and $u(\omega)$ are, respectively, the Fourier transforms of the output and input signals, and where the gain factor $f(\omega)$ is referred to as the seismometer's frequency response. Because the input $u(t)$ and output $\xi(t)$ are related in the time domain by an ordinary differential equation with constant coefficients, the frequency

[1]IRIS (*http://www.iris.edu*) "is a university research consortium dedicated to exploring the Earth's interior through the collection and distribution of seismographic data."

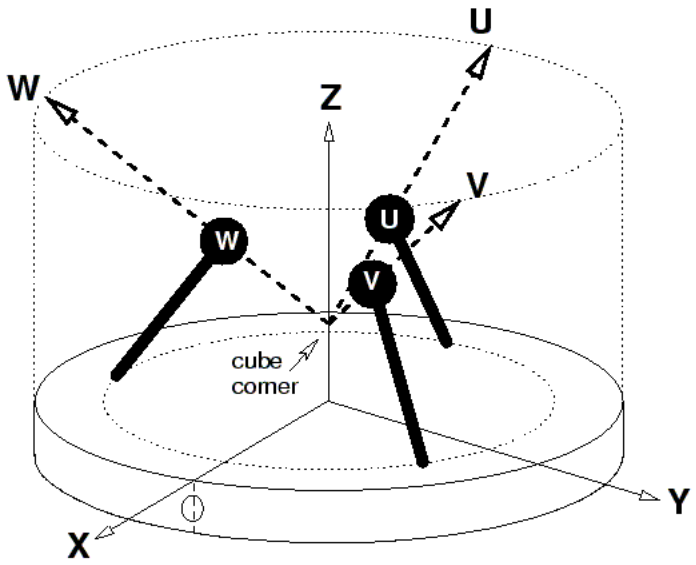

Figure 3.1: The Swiss-made STS-2 is a portable, modern force-balance seismometer in which the combined motion of three identical inertial pendulums in a cube-corner geometry (U, V, W) are resolved into motions along the three conventional orthogonal directions: east-west (X), north-south (Y), and up-down (Z), hereon referred to as E, N, and Z, respectively. In addition to its broad frequency range and its large dynamic range, the STS-2 has a robust and compact design which makes it most suitable for transportation and employment in temporal stations such as the ones built for this study. (Illustration from Wielandt, 2002.)

	Real part (rad/s)	Imaginary part (rad/s)
Poles	−0.037	+0.037
	−0.037	−0.037
	−251.3	0
	−131.0	+467.3
	−131.0	−467.3
Zeros	0	0
	0	0

Table 3.1: Poles and zeros of the STS-2's frequency response to ground velocity. The STS-2 has five poles (one real-valued and two complex conjugate pairs), and two zeros. (Poles and zeros quoted from IRIS, 2003.)

response is the quotient of two polynomials in ω, both of which can be factored and expressed in terms of their roots. The roots of the polynomial in the denominator and the roots of the polynomial in the numerator are respectively referred to as the *poles* and *zeros* of the frequency response $f(\omega)$. Moreover, because the coefficients of both polynomials are real, the poles and zeros of a seismometer are always either real or "symmetric," in the sense that they occur in complex conjugate pairs. The response of the STS-2, as well as that of any seismometer, can be completely and succinctly specified by stating the locations of the seismometer's poles and zeros (Table 3.1).

The flat frequency response of the STS-2 for over three orders of magnitude (Fig. 3.2) is the result of its near-critical damping[2] and is a very convenient feature, as accounting for instrument response distorsions when an-

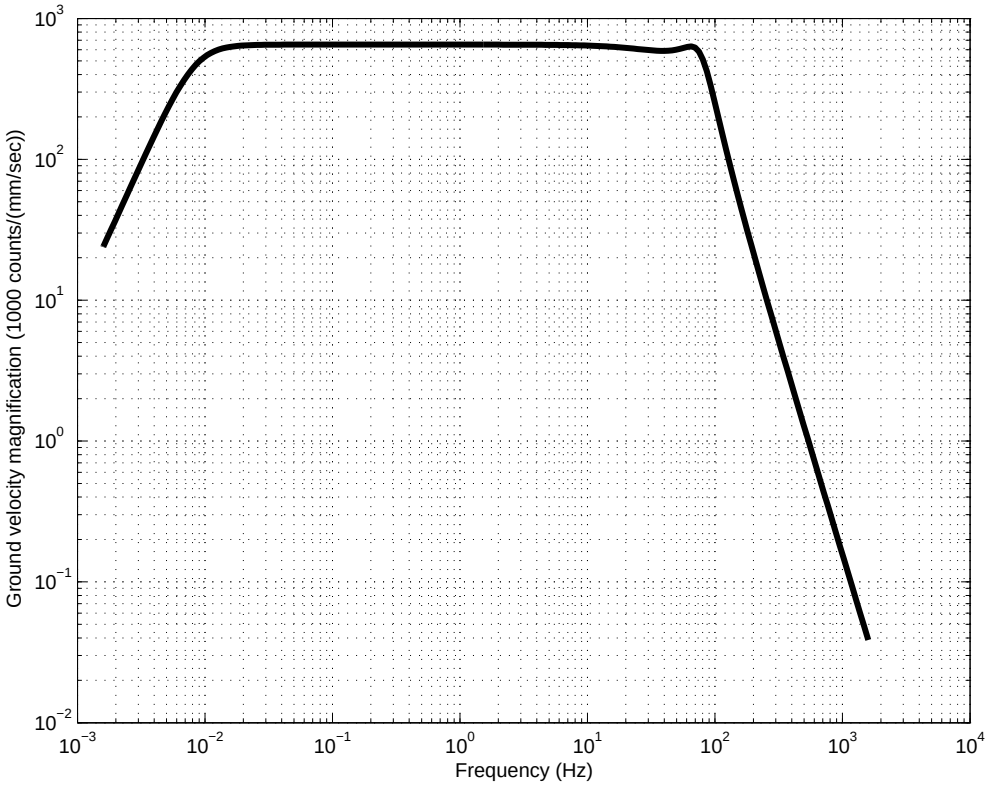

Figure 3.2: Frequency response to ground velocity of the STS-2. The STS-2 is such a versatile digital seismometer that can it record high-frequency signals from local earthquakes and active sources (*e.g.*, planned explosions or vibrations) as well as long-period teleseismic signals from distant earthquakes and other passive sources. Should both short- and long-period events of interest take place simultaneously, the digital record can be filtered to isolate the two overlapping signals.

alyzing an STS-2 seismogram reduces to filtering out those parts of the time series with frequencies in either of the two regions where the response is not flat and dividing the seismogram by the appropriate amplification factor. With a sensitivity G of 1500 mV/(mm/s) and a Q330-specified conversion factor C of 435 counts/mV, the peak ground velocity magnification of the STS-2 is GC, namely 652,000 counts/(mm/s).

The output of the STS-2 is a voltage signal whose amplitude is directly proportional to ground velocity, the constant of proportionality being the seismometer's sensitivity G. This output signal is received by the Quanterra Q330 data acquisition system, which includes an analog-to-digital converter or *digitizer*. The Q330 digitizer samples the voltage signal at constant time intervals $1/r$, where r is referred to as the *sampling rate* of the digitizer, and converts it to digital counts at C counts per mV. Although sampling involves the rejection of data between samples, by setting r to 100 SPS,*Nyquist's theorem* (*e.g.*, Bracewell, 1978) guarantees that sinusoids with frequencies under 50 Hz in the original signal are fully recoverable from the sampled time series. Moreover, 50 Hz is a convenient threshold because it approximately coincides with the highest frequency to which the STS-2 is sensitive. With its 24-bit digitizer, the Q330 can assign to each sample it takes from the analog seismometer signal an integer number of counts between -2^{23} and 2^{23}. Because a single count represents $1/GC$ mm/s, the *resolution* or smallest readable signal

[2]Critically-damped oscillatory systems allow their mass to return to its equilibrium position quicker than overdamped systems and without the undesirable oscillations caused by underdamping, and appear in such mundane applications as the suspension systems in cars and the shock absorbers on doors.

amplitude of the Q330 is on the order of 10^{-9} m/s and its maximum readable amplitude is on the order of 10^{-2} m/s, so it has a *dynamic range*[3] of ∼140 dB. The broad dynamic range of the STS-2/Q330 system makes it suitable for recording minimum global noise levels (Fig. 1.1) as well as the strong motions of large-magnitude regional earthquakes.

The noise data was stored in a local Baler14 recorder, hard-wired to the Q330, in miniSEED format, a subformat of the Standard for the Exchange of Earthquake Data (SEED), developed by the Federation of Digital Broadband Seismograph Networks. The Baler14 recorder, with a 20-GB maximum capacity, was capable of storing up to eight months of continuous data without servicing. In addition to being recorded locally, the data was radio-transmitted to the nearby Langmuir Laboratory for Atmospheric Research (Fig. 2.3) through 802.11-telemetry, from where it was re-transmitted via the Internet to the IRIS PASSCAL Instrument Center located on the New Mexico Tech campus. At New Mexico Tech, data streams received in real time were saved in Antelope, a data-managing software developed by Boulder Real Time Technologies, which organized them into daily data folders.

The timing system of each Q330 is based on a chronometer driven by a high-precision temperature-compensated quartz crystal oscillator and phase-locked to Global Positioning System (GPS) universal time through a miniature receiver. Although chronometers having GPS time as their external standard reference have been advertised as having atomic-clock accuracy, delays in the GPS signal arriving from the satellites (*e.g.*, due to atmospheric effects and multi-pathing near the ground), as well errors in the satellite orbits, translate

into perceptible timing errors. Thus, in practice, each station was synchronized with universal time and with each other with an accuracy no worse than ∼1 ms, according to Kinemetrics (2004). Just like in high-resolution studies of the earth's structure using seismic arrays, timing accuracy is crucial in the study of differential ground displacement at MRO. In fact, in the early days of our data processing, we found that when noise signals from two stations were asynchronous by as much as 500 ms, the oceanic microseism peak would still appear in the differential noise signal.

3.2 Installation

Reasonably enough, the greater the care taken during the installation of a station for data acquisition, the higher the quality of data acquired and thus the easier its processing and interpretation. With this philosophy in mind, PASSCAL and MRO staff installed, between November 2002 and April 2003, the four seismic stations indicated in Figure 2.3. Each station consisted of two vaults, one for isolating the seismometer and thus provide it with both physical security and thermal stability, and the other for hosting the recording electronics. Other essential components of each deployment were a radio transmitter for data telemetry, and a pair of solar panels for re-charging the batteries powering the station.

The vaults hosting the seismometers were parachute cargo drums: hollow steel cylinders roughly 58 cm high by 72 cm in diameter (Fig 3.3), in pits dug deep enough into the local regolith to bury the drum completely.

[3]Dynamic range (dB)= $20 \log_{10}$(maximum amplitude/resolution).

Figure 3.3: One of the four vaults hosting the seismometers is shown prior to shallow burial. Note that there is nothing particularly special about using steel cylinders to make the vaults rather than, say, a concrete box. However, old 55-gallon drums are handy almost everywhere and are commonly used in temporary deployments. The black, nearly horizontal straps secure the close-cell blue foam insulation to the outer surface of the cylinder. The short, narrow pipe protruding near the top of the vault provides an exit for the cabling. To ensure that the seismometer is thermally insulated on all sides, the bottom of the cap, shown sitting atop the vault, is also covered with a circular plate of blue foam. (Photo courtesy of Day Frostenson.)

Prior to burial, the bottom of each drum was torched off and replaced by a circular, 5-cm-thick insulating plate of close-cell blue foam. The outer curved surface of the drum was also covered in blue foam, secured to the drum with tight straps and glued to the edges of the bottom insulating plate with spray foam that quickly dried to a rigid foam. Once the drum was in the pit, a large circular opening, roughly 35 cm in diameter, was cut in the center of the bottom insulating plate, and concrete was poured through the opening to build a pad on which to sit the seismometer (Fig. 3.6). The concrete pad, which is effectively isolated from the drum walls by the insulating plate, both provided a level surface for sensor installation and enhanced the sensor's coupling to the ground. While pouring the concrete and water mix, care was taken to stir the mix to ensure that no bubbles formed that could lead to the formation of cracks after the solidification of the concrete. Once on the solid concrete pad, each seismometer was aligned with the geographic coordinates, with an accuracy of a degree or two, with the aid of a Brunton compass, and leveled with the horizontal by adjusting and subsequently locking the feet of the sensor until the bubble in the leveling chamber was centered.

The vaults hosting the recording electronics and the batteries powering the stations were large Greenlee steel toolboxes, on top of which two 65-W Solarex panels were mounted to recharge the batteries as needed. To maximize heat assimilation, the solar panels faced south, toward the equatorial line, and were tilted at approximately 50° from horizontal.[4] The seven 12 V-, 45 A·h-batteries were kept in a Rubbermaid box within the larger Greenlee toolbox. Figure 3.4 shows the inside of a Greenlee vault: the largest instrument is a Q330 digital acquisition system, fully operational between −20 and 50°C, protected

Figure 3.4: One of the four Greenlee vaults hosting the recording electronics. Clockwise from the top left: Q330 data acquisition system, Baler14 recorder, charge/load controller box, radio link, and ethernet switch. Batteries are kept in the box on which the electronics sit and are therefore not visible. Every vault was kept locked throughout the experiment to discourage vandalism. (Photo courtesy of Glen Gettemy.)

by insulating foam from the extreme temperatures to which the summit of the Magdalena Mountains may be subject; to the right of the Q330 sits the uninsulated Baler14 recorder, physically smaller but with a broader operational range of -40 to 85°C; at the far right, the charge/load controller box regulates the power delivered by the batteries so that their effective output voltage is always maintained within user-specified limits. The other small electronic devices in the figure are a Data Acquisition Modules 6520 five-port industrial ethernet switch and a Linksys wireless ethernet bridge that acts as a radio link between the wired, ethernet-equipped seismic station and Langmuir Laboratory.

With all the required cabling appropriately set up, the sensor's power supply was switched on, and the three pendulum masses of the STS-2 were unlocked and centered (Fig. 3.6). Once closed, each vault was covered with a large plastic cloth to protect it against precipitation, and with a thick wooden

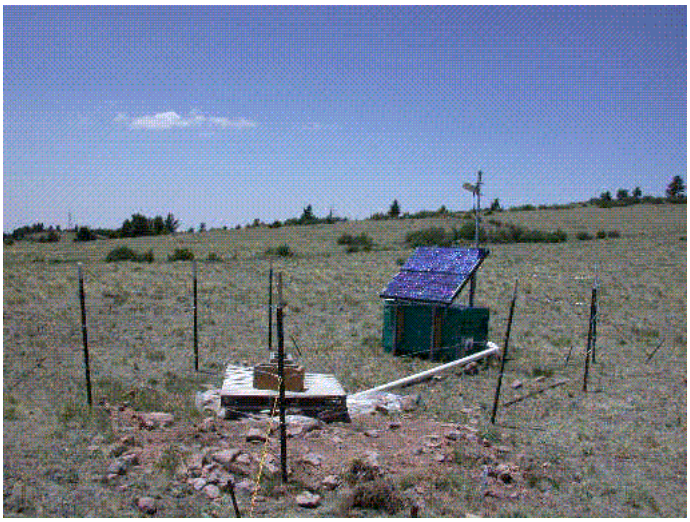

Figure 3.5: An MRO seismic station in its full glory. (Photo courtesy of Brady Romberg.)

board to minimize its direct exposure to sunlight. The less traditional choice of using plastic and wood rather than dirt for covering the vault was made on the basis of ease of accessibility in case a seismometer needed servicing during the experiment.

Figure 3.5 shows what a completed seismic station would look like to a casual hiker atop South Baldy. The STS-2 vault is completely hidden by the wooden board, held down by bricks to stop wind gusts from knocking it over. The Greenlee vault was also secured against violent wind gusts by pinning it to the ground with four long concrete stakes. The white tube bridging the two vaults is a 2.5"-diameter PVC pipe that protects the cables delivering power to the STS-2 as well as those through which the seismometer delivers

[4]The tilt angle suggested by Solarex is the local latitude (°) plus 15°.

Station	Latitude (°)	Longitude (°)	Altitude (m)
CNTR	33.9782	-107.1870	3187
NELG	33.9793	-107.1858	3183
SWLG	33.9766	-107.1864	3186
NWLG	33.9789	-107.1888	3190

Table 3.2: GPS coordinates of the four seismic stations (*cf.* Fig. 2.3). Latitudes and longitudes are accurate down to a few meters (i.e., a few ten-thousandths of a degree). Although there is a somewhat larger uncertainty in the altitude measurements (*cf.* USGS-based topography in Fig. 2.3), all four stations lie on approximately the same horizontal plane. Stations are named according to their position within the Y-shaped seismic array: stations at the ends of the northeast, northwest, and southwest legs of the array are named NELG, NWLG, and SWLG, respectively; the station at the center of the array is named CNTR.

data to the Q330. The long, upright, metallic pole attached to the Greenlee vault holds both the white cylinder that is the Astron radio transmitter as well as the black, miniature GPS antenna manufactured by Trimble. The radio transmitter points toward Langmuir Laboratory, approximately 0.6 km from the center of the seismic array, while the magnetically-mounted GPS antenna provides not only a very accurate absolute time reference but also very accurate geographical coordinates for the site (Table 3.2). The fence built around each station in June 2003, half-way through the data acquisition period, consists of barbed wire on metallic T-posts and protected the experiment from cultural interference, including humans (*e.g.* hikers and campers) and local fauna (*e.g.*, deer and cows).

Evidently, a crucial requirement for a consistent analysis of the seismic

Figure 3.6: Centering of an STS-2 inside a completed vault just prior to capping. The three pendulum masses are centered by pushing a button on the small green box shown (manipulated in the photo by PASSCAL's Tim Parker), and then verifying that the mass-position voltages read off the Flukemeter are within 2 V of zero. The orange cable shown is wrapped around the sensor once completely and then secured onto the blue foam insulation at two points opposite each other to reduce the coupling of noise to the STS-2 when the cable is subject to thermal variations. (Photo courtesy of Dan Klinglesmith.)

data collected by an array is that all stations making up the array be identical to each other. Long-term testing of sensors and electronics at the PASSCAL Instrument Center has shown that their STS-2 seismometers behave comparably (*e.g.*, their sensitivities have been measured to be indeed within a few percent of 1500 mV/(mm/s), which is the value advertised by the manufacturer). However, some of the differences among stations built are beyond the control of the builder; for instance, the geology of all sites in which vaults are buried may not be precisely the same, and this may introduce caveats in the interpretation of data. Fortunately for this study, it is actually useful to record any shallow-geology-triggered differences in seismic noise levels between any two stations because these reflect the different degrees of motion to which the telescopes will be subject in each site once they are put in place. Geology-related noise is thus more of a contribution than an obstacle to our study of relative ground displacements between future telescope sites. On the other hand, a seismic array designed to image the fine structure of the subsurface to a depth of a few hundred meters or so will deem these differences in shallow geology as undesirable. (In any case, recall that in Chapter 2 we concluded that the shallow geology to a depth of at least 35 ft is essentially the same at the location of all four MRO seismic stations and thus should not be responsible for any difference in seismic response from station to station.) Of the small controllable differences among the MRO stations built, perhaps the most relevant is the extra protection against thermal convection in CNTR and NELG. Although sunlight-delivered heat reaching the vault from the surrounding soil by conduction (and, thence, reaching the seismometer by convection within the open spaces in the vault) is minimized by insulating the vault in its entirety,

electronic seismometers themselves dissipate a small amount of heat. To minimize thermal convection due to this "autogenic"heat, the sensors in CNTR and NELG were each enclosed by a bottomless box of 5-cm-thick extruded polystyrene, held firmly in place by a cardboard box that fit tightly between the top polystyrene face and the cover of the vault. Another small difference in vault construction consisted in sitting the STS-2 in SWLG on a 30 cm by 30 cm paving stone rather than directly on the cement pad, which was not leveled with the horizontal because of the inclined topography at that particular site (Fig. 5.5). Otherwise, all four seismic stations built were essentially identical to each other. Minor differences in installation are expected to have an impact neither on the quality of the data collected nor on the consistency of the noise data analysis presented herein.

CHAPTER 4

DATA PROCESSING

4.1 Data coverage

The database used in this study covers the thirty-six weeks between the second week of February and the fourth week of October 2003, effectively including data from all four seasons of the year. With each station contributing three streams of continuous noise velocities during this eight-month period (one stream from each of its three components of motion, Z, N, and E in Fig. 3.1), the database comprises twelve continuous 100-SPS data streams which were archived by day in the Antelope data-managing system at New Mexico Tech. Together with the noise data recorded simultaneously at a lower sampling rate (not used in this study) and the continuous data corresponding to the state-of-health channels of each station (mass-positions, power, etc.), the size of the complete database has been estimated at about 25 GB, roughly 80% of which is comprised by the 100-SPS noise data set analyzed in this study.

4.2 Characteristic background noise periods

Because, as mentioned earlier, it is noise faster than 1 Hz which poses the greatest challenges for active optical systems, and because night-time hours will be the most useful to astronomers at MRO (since their studies will center upon celestial objects other than our Sun), data processing in this study focused

on noise with frequencies above 1 Hz observed during the hours between sunset and sunrise in New Mexico. The upper limit of the frequencies observed ($\sim$50 Hz) was dictated by our seismometers (Fig. 3.2).

The three characteristic noise periods identified in each of the 36 weeks studied are the three hours of, respectively, maximum, minimum, and median background noise within each week. Out of these three sets of characteristic hours, the set of 36 maximum noise hours are analyzed in detail, in an effort to delineate the worst-case noise situations observed at the site. In determining the maximum, minimum, and median noise periods of each week, transient phenomena (*e.g.*, earthquakes) were not removed from the data and, because of the comparatively short duration of most such phenomena, were expected not to bias the hourly noise averages to a large extent. Transient phenomena which were found to cause bias in the hourly background noise averages at the site, as well as those not directly observed but thought to have the potential to cause such effect, are investigated separately in this study.

The three characteristic noise hours of each week were picked from among a hundred or so night-time hours by using the root-mean-square (RMS) noise velocity of each hour to quantify its noisiness. However, because not all four stations usually agreed unanimously on which hour of the week had the largest RMS velocity (and sometimes not even the three components of motion within individual stations agreed on the noisiest hour), each of the twelve components making up the seismic array was given the right to issue a "vote" and the noisiest hour of the week was then chosen "democratically." The minimum and median noise hours of the week were picked in a similar

fashion. This method of identifying the characteristic noise hours is particularly appropriate for identifying the noisiest hour of the week because it helps to discriminate between station-specific maxima (*e.g.*, trucks passing close to one station only) and site-specific maxima (*e.g.*, a regional earthquake affecting the entire array); the latter would be more likely than the former to cause two or more stations to agree on the maximum noise hour, which would then be identified as such by the democratic method. We would subsequently be able to make a better estimate of the maximum differential noise between stations, which, as mentioned earlier, is more relevant to this study than maximum station-specific noise.

The semi-automated scheme designed to identify the characteristic noise hours worked as follows:[5] For each station component (Z, N, and E) a continuous 36-week database of noise velocity records was available, the night-time periods of which were split into 1-hour data files and converted to the MATLAB-friendly Seismic Analysis Code (SAC) format with a brief Bash script based on Antelope's **trexcerpt** function; these 1-hour noise velocity files were subsequently grouped into weeks and exported to MATLAB, where all other stages of data processing were performed; upon subtracting its mean and removing any linear trend within, each 1-hour data file was high-pass filtered at 1 Hz and had its RMS noise velocity computed and grouped with the RMS velocities corresponding to hours of the same week. The filter used was a fourth-order Butterworth digital filter with a reasonably sharp transition between pass band and stop band. With a week typically consisting of a hundred or so night-time hours, the three characteristic noise hours of the week were identified with MATLAB's **max**, **min**, and **median** commands, which respec-

tively singled out from the hundred or so RMS values the highest, lowest, and median noise velocities of the week as sensed by a particular station component (the Z-component, say). Upon following this procedure for all twelve station components, "votes" were counted and the final decision as to which were the characteristic noise hours of the week was reached. Minor problems with the data-acquisition equipment were not absent during some weeks, in which cases each station component had fewer than a hundred "candidates" to choose from when deciding on the characteristic noise hours.

Although we picked the characteristic noise periods of each week based on recorded RMS velocities, the interest of this study is really on RMS *displacements*, as our goal is to find out whether or not seismic noise at the site results in ground displacements within acceptable levels. Nevertheless, picking the maximum, minimum, and median noise periods of each week using velocities rather than displacements saved precious processing time, for we avoided integrating each of the nearly forty thousand 1-hour velocity seismograms involved in identifying all characteristic noise periods in the 36 weeks covered by the study. The underlying assumption that using displacements to do the identification would have resulted in the same picks that we obtained using velocities is based on the fact that velocities can be thought of as displacements upon which the differential operator d/dt has acted and, since this operator is linear, velocity can be thought of as being directly proportional to displacement in the

[5]To automate as much as possible the process of plotting spectra and computing RMS displacements from the hundreds of raw, unfiltered noise velocity files corresponding to the characteristic noise periods of each week, the author, in collaboration with PASSCAL intern Brady Romberg (now at Colorado School of Mines), developed relevant MATLAB functions in the summer of 2003.

sense that doubling the velocity doubles the displacement, halving the velocity halves the displacement, and so on.

While in Chapter 5 we have estimated the interferometer's operational downtime based upon hourly RMS displacements recorded, these hourly averages underestimate the occurrence of peak transients in the ground motion field. Peak transients with amplitudes larger than about 25 nm (even those lasting just a few milliseconds) can compromise the operation of the interferometer, since the astronomical data to be acquired will be, to a first approximation, collections of independent 10- to 100-ms exposures, and it is over such time intervals that optical pathlengths (section 1.4) must be stable for fringe measurements to be performed. (The observation of a star typically lasts some 100 seconds and consists of 10^3 to 10^4 fringe measurements.) Nevertheless, the only peak transients of concern for interferometry that are likely to be underestimated by the hourly RMS averages are those related to local earthquake activity. We deal with the issue of local earthquake activity in section 5.2.1.

4.3 PSD plots and RMS displacements

Displacement PSD plots display the power spectrum associated with the ground motion of the individual stations (*e.g.*, Fig. **??**), thereby allowing us to determine at which frequencies seismic noise exhibits most power. Differential displacement PSD plots display the power spectrum of the difference in ground motion between pairs of corresponding station components (*e.g.*, the Z-component of CNTR and NELG) and are of most interest, as it is differential movement that will lead to noticeable optical-path fluctuations (section 1.2). Displacement and differential displacement PSD plots were produced for the

three characteristic noise periods of each week. The complete set of spectral plots for all 36 weeks studied is included in Appendix B. PSDs were computed and plotted in MATLAB using Welch's averaging method (Welch, 1967) with a Hanning taper and 375-s windows with 50% overlap. The Hanning taper was chosen because it provides a reasonable trade-off between reduction of power leakage and loss of spectral resolution.

RMS displacements are calculated to determine whether or not seismic noise results in ground motion within acceptable levels and are thus central to this study. RMS displacements for each station and RMS differential displacements for each pair of corresponding station components (*e.g.*, the N-component of SWLG and NWLG) were computed for the three characteristic noise periods of each week by numerically integrating the corresponding PSDs between 1 Hz and ∼50 Hz. All RMS displacement values computed are tabulated in Appendix C. Each table consists of three columns showing RMS displacements with frequencies above 1 Hz, 2 Hz, and 5 Hz, respectively. For each station, a plot of maximum 1-hour RMS displacement (> 1 Hz) versus time of the year is shown in the next chapter (Fig. 5.2).Plots of median and minimum 1-hour RMS displacements (> 1 Hz) versus time of the year are also shown for comparison (Fig. 5.3 and Fig. 5.4); in fact, while the analysis of worst-case noise conditions at the site will be most useful to the engineers in charge of *building* the interferometer, median noise conditions will be of much interest to the astronomers who will be *operating* it.

Although RMS displacement tables exclude displacements associated with frequencies below 1 Hz, displacement PSD plots display power throughout

the recording range of the STS-2 seismometers (120 s to ∼50 Hz) in order to compare the PSD plots produced with the complete global high and low noise models, including the oceanic microseism region, which peaks at about 7 s (∼0.14 Hz) and 14 s (∼0.07 Hz). This was done to verify the normal behavior of the MRO noise data: because oceanic microseisms are the strongest naturally-generated source of seismic background noise, in the absence of transients (*e.g.*, prominent surface waves with periods around 15 s from a distant, shallow earthquake) the power spectral curves of well-behaved MRO noise data are required to mimic the oceanic microseism curve. On the other hand, it would have been harder to recognize atypical behavior in noise data caused by a flaw in the recording system or to pick up a flaw in the data processing scheme by looking at PSD plots in the more restricted frequency range between 1 and 50 Hz, since noise faster than 1 Hz is mainly due to local activity (*e.g.*, wind and cultural noise) and lacks a standard to be compared against, as the global noise models themselves truncate at just 10 Hz.

4.4 Wind during the noisiest hour of each week

To investigate the possible correlation between wind activity and background noise at the MRO site, the median wind speed during the noisiest 1-hour period of each week was computed and included in the plots of maximum 1-hour RMS displacement versus time of the year mentioned in the previous section. Note that the weekly wind speeds reported are not necessarily the maximum wind speeds of the week at the site; they are just the wind speeds measured during the hour of maximum *seismic* noise there.

Weather data was obtained from the MROST weather station located

just southwest of the building on South Baldy hosting the Joint Observatory for Cometary Research (Fig. 2.3). The station consists of a Campbell Scientific Instruments system with sensors to measure the speed and direction of the wind, in addition to other weather parameters, and with a data logger that samples information at 1-min intervals. The median wind speed during any particular hour was simply obtained by finding the median of the 60 samples corresponding to that hour. Median wind directions were computed in a similar way and the undesirable effect caused by the wrapping of direction values at the end points of the measuring range (namely 0° and 360°) was dealt with by mapping the values into a suitable range prior to taking the median. Standard deviations from the average wind speeds and wind directions were also computed and reported. The complete set of wind statistics is included in Appendix D. When the MROST weather station was down (on 7 out of the 36 weeks studied), weather data was obtained from the station in Dr. Carl Popp's trailer, MROI, at the south end of the Magdalena Ridge (Fig. 4.1), which consists of a Davis Instruments system that samples data at 30-min rather than 1-min intervals and reports mean wind speeds and mean wind directions rather than medians.

Figure 4.1: A trailer parked at the south end of Magdalena Ridge (see Fig. 2.3 for a map view) hosts Dr. Carl Popp's weather station, MROI Although most weather data used in this study is MROST data, MROI provided wind speeds and directions whenever MROST was not operational. (Photo courtesy of Day Frostenson.)

CHAPTER 5

RESULTS AND ANALYSIS

The thirty-six weeks upon which seismic noise characterization at the MRO site is based are weeks 7 through 42 of 2003 (mid-February through late October), where the weeks of the year are numbered as in Table 5.1. Thus, all four seasons of the year are well-represented in the database (Fig. 5.1). Results and their corresponding analysis are divided into two main sections: seismic background noise (i.e., noise resulting from *continuous* seismic activity), with emphasis on the maximum ground displacements that can be observed at the site as well as on the correlation between wind activity and these maxima; and transient noise (i.e., noise resulting from *finite-duration* seismic phenomena) due to earthquakes, traffic, and machinery. Results and analyses are all for night-time noise in the high frequency part of the spectrum (1 to 50 Hz), unless otherwise specified.

5.1 Seismic background noise

5.1.1 Most likely maximum ground displacements

The goal of this study is to give astronomers at MRO an idea of how troublesome, if at all, seismic noise will be for their observations on any given night of the year. For this purpose, we have analyzed Table 5.2, which exhibits measured ground displacements, using a simple probabilistic approach. In this

Figure 5.1: Winter at the MRO site during the data acquisition period. New Mexico Tech geophysics professor Rick Aster services a station after a snowstorm. The data analyzed in this study was recorded during the last six weeks of winter, through the spring, the summer, and the first four weeks of autumn: a total of thirty-six weeks. (Photo courtesy of Rick Aster.)

Week	Dates	Remarks
1	January 1 - January 7	
2	January 08 - January 14	
3	January 15 - January 21	
4	January 22 - January 28	
5	January 29 - February 04	
6	February 05 - February 11	CNTR and NELG begin recording
7	February 12 - February 18	
8	February 19 - February 25	
9	February 26 - March 04	
10	March 05 - March 11	
11	March 12 - March 18	SWLG begins recording
12	March 19 - March 25	Winter ends/Spring begins
13	March 26 - April 01	
14	April 02 - April 08	Windy season begins
15	April 09 - April 15	
16	April 16 - April 22	
17	April 23 - April 29	NWLG begins recording
18	April 30 - May 06	
19	May 07 - May 13	
20	May 14 - May 20	Windy season ends
21	May 21 - May 27	
22	May 28 - June 03	
23	June 04 - June 10	
24	June 11 - June 17	
25	June 18 - June 24	Spring ends/Summer begins
26	June 25 - July 01	
27	July 02 - July 08	Monsoon season begins
28	July 09 - July 15	
29	July 16 - July 22	
30	July 23 - July 29	
31	July 30 - August 5	
32	August 6 - August 12	
33	August 13 - August 19	
34	August 20 - August 26	
35	August 27 - September 2	Monsoon season ends
36	September 3 - September 9	
37	September 10 - September 16	
38	September 17 - September 23	Summer ends/Autumn begins
39	September 24 - September 30	
40	October 1 - October 7	
41	October 8 - October 14	
42	October 15 - October 21	
43	October 22 - October 28	Data acquisition ends

Table 5.1: Convention adopted in this study for numbering the weeks of 2003.

Week	CNTR			NELG			SWLG			NWLG		
	N	E	Z	N	E	Z	N	E	Z	N	E	Z
7	4	4	7	3	4	2	-	-	-	-	-	-
8	5	5	8	2	3	2	-	-	-	-	-	-
9	3	3	5	3	4	2	-	-	-	-	-	-
10	2	3	2	3	4	2	-	-	-	-	-	-
11	5	5	9	3	3	3	6	5	10	-	-	-
12	3	4	5	3	3	2	2	2	4	-	-	-
13	3	3	4	2	3	2	3	3	7	-	-	-
14	8	6	14	4	5	4	10	12	22	-	-	-
15	7	6	11	4	5	3	7	9	16	-	-	-
16	8	8	11	6	9	7	6	9	14	-	-	-
17	8	7	12	4	5	4	-	-	-	3	3	3
18	7	6	12	3	4	4	-	-	-	2	2	2
19	5	5	8	3	4	2	-	-	-	3	3	4
20	7	6	9	5	5	4	-	-	-	4	5	5
21	30	33	13	18	20	12	-	-	-	12	20	7
22	2	2	3	2	2	2	-	-	-	1	1	1
23	3	2	2	1	1	1	4	4	4	2	1	1
24	51	51	22	39	36	19	42	51	17	24	35	15
25	44	50	25	43	33	23	45	60	25	22	37	21
26	3	2	3	1	2	1	4	5	5	2	2	1
27	3	2	3	1	1	1	4	4	5	2	2	2
28	2	2	2	1	1	1	2	2	2	1	1	1
29	4	3	5	2	2	1	6	6	8	3	3	2
30	3	2	3	1	1	1	4	4	4	2	2	2
31	2	1	2	1	1	1	2	3	3	1	1	1
32	5	5	6	5	4	4	4	5	5	2	2	2
33	15	20	10	15	19	10	18	22	9	-	-	-
34	8	8	11	4	4	4	1	1	1	1	1	1
35	4	4	5	2	2	3	4	5	5	2	2	2
36	3	2	3	2	2	1	2	3	3	-	-	-
37	29	13	29	3	2	1	2	2	1	-	-	-
38	2	2	2	2	2	1	3	3	3	-	-	-
39	2	2	2	1	2	1	2	2	2	1	1	1
40	2	2	2	1	1	1	2	2	2	1	1	1
41	25	20	11	43	37	20	6	7	5	5	5	3
42	4	3	4	2	2	1	5	5	6	3	3	3

Table 5.2: Maximum RMS ground displacements observed at MRO during the entire study period. Each number represents ground motion averaged over one hour and rounded up to the nearest nm.

table, each row corresponds to a week of the year and includes twelve ground displacement values, one from each station component. Ground displacements here are averages of ground motion over the noisiest hour of each week studied, and are rounded up to the nearest nm. For each of the twelve components (columns) in the table, we have built a frequency table to show which displacements are measured most commonly by each component in the 36-week period. Table 5.3 is an example of one such frequency table. Because this frequency table is derived from Table 5.2, where displacements are rounded up to the nearest nm, the first column in the frequency table shows displacement *ranges* rather than discrete displacements. The second column of the table shows the number of times each displacement (range) was the maximum displacement recorded during the 36 weeks studied and adds up to 36, and the third column shows the same value as the second but expressed as a percentage of the total number of weeks studied and adds up to 100. It is clear from the frequency table for the vertical component of NELG that there is a "cluster" of ranges, toward the top of the table, that represents the displacements that are most likely to be recorded by this one component on any particular night of the year: displacements between 0 and 4 nm were observed to be the maximum displacements on 30 of the 36 weeks studied. This can be interpreted as follows: assuming that 2003 was a typical year in terms of ground motion at the MRO site, there is an 83% probability that, during any one hour on a particularly *noisy* night between February and October of any future year, the average vertical displacement at the deployment location of NELG will not exceed 4 nm. Applying this same reasoning to the frequency tables of the other 11 station components, and defining a "cluster of ranges" in a frequency table to be

a group of three or more consecutive nonzero-frequency ranges with no two ranges being separated by more than one zero-frequency range, we have built Table 5.4. This table should be of more interest to astronomers, for it places upper bounds on the most likely amplitudes of ground motion that will be observed at the MRO site on the noisiest nights of the year: ground displacements at any of the four station locations typically (i.e., on $\sim 85\%$ of occasions) will not exceed 14 nm and will be, on average, 7 to 8 nm. Obviously, the most likely maximum ground displacements predicted for quieter nights are smaller.

The reader will have probably noticed that five or six rows in Table 5.2 jump out of the page because of their double-digit displacements (weeks 21, 24, 25, 33, 37, and 41). These abnormal ground displacements, which in turn correspond to abnormal peaks in Figure 5.2 (labeled **a** through **f**), were all caused by transient phenomena that will be treated in some detail later in this study (subsection 5.1.4 and section 5.2). Note that these strong transient phenomena are relatively rare occurrences. For example, they cause double-digit displacements in the vertical component of motion of NELG only on 5 out of the 36 weeks studied and, although these displacements are not among the most likely displacements that will be observed at this station on any given noisy night (Table 5.4), there is still a probability of $\sim 14\%$ that they will be observed at NELG on any such night.

We have thus chosen to characterize the most likely maximum ground displacement recorded by a station component in terms of the *cluster* of displacement ranges most observed in the frequency table of the component rather than in terms of the *single* most observed displacement range in the table, which

would have been a reasonable alternative parameter upon which to base the characterization. For example, in the case of the vertical component of NELG, the single most observed displacement range is the 0-to-1-nm range, which is observed in 13 out of the 36 weeks studied. However, the cluster approach is favored over this other parameter for two reasons, which we explain while still taking the vertical component of NELG as an example. Firstly, in any one or more of the 13 displacement observations made by this component that fall in the 0-to-1-nm range, there is an inextricable uncertainty in the displacement measurements in the sense that any of the 13 "true" displacements could have been just above 1 nm. If we just took the 0-to-1-nm range as our parameter for characterizing the most likely maximum ground displacement sensed by the component in question, we would say that there is a 36% probability that on any future night between February and October the vertical component of ground motion at the deployment site of NELG will be at most 1 nm. However, not only is the probability associated with this prediction rather small, but measurement uncertainties also make it inaccurate. On the other hand, the cluster approach accounts for these uncertainties by taking into account in the analysis the ranges neighboring the most frequent range. Thus, by characterizing the most likely ground displacement in terms of a larger displacement range (0 to 4 nm), which is associated with a larger probability of occurrence (83%), the cluster approach is more likely to correctly predict maximum noise levels. The second reason for preferring the cluster approach is purely practical: characterizing most likely maximum ground displacement with a larger displacement range typically results in a higher upper bound for the maximum displacement and thus gives the astronomer a worse-case noise scenario than

one which a smaller displacement range would give. Our emphasis on worse-case noise scenarios in this study will be useful not only to astronomers, who wish to know the particular times during which it will not be recommendable to operate the interferometer, but also to engineers in charge of designing the telescope buildings and who will need to decide on the appropriate degrees of stiffness and damping for the structures.

5.1.2 Most likely maximum differential ground displacements

In the same way that maximum ground displacements are displayed in Table 5.2, maximum *differential* ground displacements are displayed in Table 5.5. Each row in this table pair, which can be thought of as one big table, corresponds to a week of the year and includes eighteen differential ground displacement values, one from each pair of corresponding station components. Differential ground displacements here are averages of ground motion over the noisiest hour of each week studied, and are rounded up to the nearest nm. Note that the same double-digit displacements of Table 5.2 (weeks 21, 24, 25, 33, 37, and 41) still jump out in this table of differential displacements, although their magnitudes have been either reduced or enhanced, depending on the nature of the transient phenomena that triggered the motion (section 5.1.4): for example, in week 25 a strong distant earthquake with epicenter in the Amazon caused the displacement from station to station to be fairly coherent,[6] so differential displacements are observed to be at most as large as (but typically smaller than) individual displacements (see Fig. 5.7 for an illustration; see Fig. 5.8 for an exception); on the other hand, machinery

Range (nm)	Counts	Percentage
0-1	13	36.11
1-2	8	22.22
2-3	3	8.33
3-4	6	16.67
4-5	0	0.00
5-6	0	0.00
6-7	1	2.78
7-8	0	0.00
8-9	0	0.00
9-10	1	2.78
10-11	0	0.00
11-12	1	2.78
12-13	0	0.00
13-14	0	0.00
14-15	0	0.00
15-16	0	0.00
16-17	0	0.00
17-18	0	0.00
18-19	1	2.78
19-20	1	2.78
20-21	0	0.00
22-23	1	2.78
Total	36	100.00

Table 5.3: Frequency table for the maximum hourly RMS ground displacements recorded by the vertical component of NELG between mid-February and late October 2003. The topmost four ranges, 0-to-1 nm through 3-to-4 nm, make up a "cluster" of ranges that concentrates $\sim$83% of the observations during the 36 weeks studied. This can be interpreted as there being an 83% probability that the maximum hourly RMS vertical displacement at the location of this station will, on any night between February and October of any future year, lie somewhere between 0 and 4 nm.

	CNTR			NELG		
	N	E	Z	N	E	Z
Displacement (nm)	8	8	14	6	5	4
Probability (%)	83.33	83.33	91.67	86.11	83.33	83.33
	SWLG			NWLG		
	N	E	Z	N	E	Z
Displacement (nm)	7	9	10	5	5	7
Probability (%)	84.62	84.62	80.77	86.36	86.36	90.90

Table 5.4: Most likely maximum RMS hourly ground displacements and their probabilities of occurrence on any night between February and October post-2003.

and traffic in week 41 caused the displacement from station to station to be incoherent, so differential displacements are observed to be at least as large as (but very often larger than) individual displacements.

The last table we present (Table 5.6) is perhaps the most relevant, for it predicts the differential ground displacements that will typically be observed during the noisiest hour on any future night between February and October. Just like Table 5.4 of most probable maximum ground displacements, Table 5.6 was built using a simple probabilistic analysis based on the cluster approach.

Had we not directly measured differential ground displacements between corresponding station components, we would have still been able to com-

[6] "A set of waveforms is coherent if the phase change from one to the next has a well-defined relationship" (Sheriff, 1973).

Week	CNTR-NWLG			CNTR-NELG			CNTR-SWLG		
	N	E	Z	N	E	Z	N	E	Z
7	-	-	-	4	5	7	-	-	-
8	-	-	-	5	5	8	-	-	-
9	-	-	-	4	4	6	-	-	-
10	-	-	-	3	4	3	-	-	-
11	-	-	-	5	5	9	7	6	13
12	-	-	-	3	4	5	3	4	6
13	-	-	-	3	3	4	4	4	8
14	-	-	-	8	7	14	12	13	26
15	-	-	-	7	7	11	10	10	19
16	-	-	-	9	10	13	9	11	17
17	8	7	13	8	7	13	-	-	-
18	8	6	12	8	7	12	-	-	-
19	6	5	9	6	5	8	-	-	-
20	8	7	10	7	7	10	-	-	-
21	29	32	12	36	34	12	-	-	-
22	2	2	3	3	2	3	-	-	-
23	3	2	3	3	2	2	4	4	5
24	41	44	18	43	49	21	41	48	20
25	32	38	10	28	34	10	27	55	11
26	3	2	3	3	2	3	5	5	5
27	3	3	3	3	2	3	5	5	5
28	2	2	2	2	2	2	2	2	3
29	5	4	5	4	3	5	7	7	9
30	3	3	3	3	2	3	4	4	5
31	2	2	2	2	1	2	3	3	3
32	5	5	6	7	6	7	6	6	8
33	-	-	-	12	11	4	9	15	4
34	8	8	11	9	9	11	8	8	11
35	4	4	5	4	4	5	5	6	7
36	-	-	-	3	2	3	3	3	4
37	-	-	-	29	13	29	29	13	29
38	-	-	-	2	2	2	3	4	3
39	2	2	2	2	2	2	2	2	3
40	2	2	2	2	2	2	3	3	3
41	25	21	12	49	43	23	25	21	12
42	5	4	4	4	3	4	6	6	7

Week	NELG-NWLG			SWLG-NWLG			NELG-SWLG		
	N	E	Z	N	E	Z	N	E	Z
7	-	-	-	-	-	-	-	-	-
8	-	-	-	-	-	-	-	-	-
9	-	-	-	-	-	-	-	-	-
10	-	-	-	-	-	-	-	-	-
11	-	-	-	-	-	-	6	6	10
12	-	-	-	-	-	-	3	4	5
13	-	-	-	-	-	-	4	4	7
14	-	-	-	-	-	-	10	13	22
15	-	-	-	-	-	-	8	10	16
16	-	-	-	-	-	-	8	12	16
17	4	5	5	-	-	-	-	-	-
18	4	4	4	-	-	-	-	-	-
19	4	4	4	-	-	-	-	-	-
20	6	6	6	-	-	-	-	-	-
21	20	20	12	-	-	-	-	-	-
22	2	2	2	-	-	-	-	-	-
23	2	2	1	4	4	4	4	4	4
24	36	46	20	37	53	19	41	56	20
25	34	34	12	41	71	16	47	61	16
26	2	2	1	4	5	5	4	5	5
27	2	2	2	4	4	5	4	4	5
28	2	2	1	2	2	2	2	2	2
29	3	3	3	6	7	8	6	7	8
30	2	2	2	4	4	5	4	4	4
31	1	1	1	2	3	3	2	3	3
32	5	4	4	5	5	5	7	6	6
33	-	-	-	-	-	-	17	22	6
34	4	4	4	1	1	1	4	4	4
35	3	3	3	5	5	5	5	5	5
36	-	-	-	-	-	-	3	3	3
37	-	-	-	-	-	-	3	3	2
38	-	-	-	-	-	-	3	4	3
39	2	2	1	2	2	2	2	2	2
40	1	1	1	2	2	3	2	3	3
41	43	37	20	7	9	5	43	38	21
42	3	3	3	6	6	6	5	6	6

Table 5.5: Maximum differential RMS ground displacements observed at MRO during the entire study period. Each number represents ground motion averaged over one hour and rounded up to the nearest nm.

pute upper bounds for these displacements from our measured ground displacements at the individual stations by assuming that in the hour during which each station component observes its most likely maximum RMS ground displacement (Table 5.4) its noise signal is both coherent and exactly out of phase with respect to the noise signals from the other three corresponding station components, so that if we computed the *differential* hour-long time series from any two corresponding station components (say, the vertical components of CNTR and NELG), our result would exhibit amplitudes *larger* than those in any of the two original time series. Moreover, by assuming that the two station components are exactly out of phase rather than only slightly out of phase, we ensure that their differential time series has amplitudes as large as possible and thus recreate the worst-case scenario.

The bottom line is good news: differential ground displacements between any pair of corresponding station components at the MRO site will typically be at most 15 nm (9 to 10 nm, on average) on any of the noisiest nights of the year. It is also clear from Table 5.6 that the probability that the differential displacements observed are in the 0-to-15-nm range is, on average, $\sim 82\%$.

It cannot be overemphasized that differential ground displacements are of most interest in this study because, as mentioned earlier, a crucial requirement of interferometry is that the optical paths from all telescopes match accurately in order to obtain a sharp and stationary interference pattern, and any differential ground motion exceeding $\sim$25 nm will conspire against this purpose. In fact, interferometry would still work if any pair of telescope sites had ground displacements in excess of 25 nm as long as their relative displace-

	CNTR-NELG			CNTR-SWLG		
	N	E	Z	N	E	Z
Displacement (nm)	9	13	14	12	15	13
Probability (%)	83.3	88.9	91.7	84.6	88.5	80.8
	CNTR-NWLG			NELG-SWLG		
	N	E	Z	N	E	Z
Displacement (nm)	8	8	6	10	7	10
Probability (%)	81.8	81.8	59.1	84.6	73.1	76.9
	NELG-NWLG			SWLG-NWLG		
	N	E	Z	N	E	Z
Displacement (nm)	6	6	6	7	9	8
Probability (%)	81.8	81.8	72.7	87.5	87.5	87.5

Table 5.6: Most likely maximum differential RMS ground displacements and their probabilities of occurrence on any night between February and October post-2003.

ment was less than 25 nm. Suppose, for instance, that during an extremely noisy hour (perhaps featuring a strong regional earthquake), a telescope at the deployment location of CNTR senses an average vertical ground displacement of 50 nm while the telescope at the deployment location of NELG senses an average vertical ground displacement of 46 nm. Assuming the motion at both stations to be coherent and exactly in phase, the differential ground displacement will be a mere 50 nm−46 nm=4 nm and will not visibly disturb the fringe pattern. Moreover, *any* arbitrarily large displacement at any telescope site would, in theory, pose no problem for interferometry as long as relative displacements remain below 25 nm. And even relative displacements exceeding 25 nm would not be a problem as long as they are slower than about 1 Hz, which is the highest frequency of motion that adaptive optics systems can compensate for. In fact, in the highly unlikely and undesirable case that long-term regional tectonic processes cause a telescope location to be uplifted a few mm and a different telescope location to *subside* a few mm in the course of a year, the optical-path lengths of the two telescopes would differ from each other by a huge amount relative to their original difference a year earlier, but the uplifting and subsiding processes would be so slow that they would, in theory, cause no problem for interferometric observations.

Although not as crucial to interferometry as differential displacements, we have seen that absolute displacements are useful to place upper bounds on differential displacements. In the first example of the above paragraph, were motion at both stations exactly out of phase rather than exactly in phase, their average differential displacement over that hour would be 50 nm−(−46 nm)=96 nm, and this would be the upper bound on their differen-

tial displacement. Were motion at both stations somewhere between exactly in phase and exactly out of phase, their average differential displacement would be somewhere between 4 and 96 nm.

5.1.3 Wind speed vs. maximum ground displacement

Figure 5.2 shows the median wind speed (solid line) and RMS ground displacement for the noisiest hour of each week between February and October 2003 (weeks 7 to 42). For instance, because the seismically noisiest nighttime hour of week 42 was determined to be the one between 8:00 and 9:00 pm (MST) on October 17, the median wind speed during that hour was computed and plotted here, although the hour in question is not necessarily the hour exhibiting the fastest wind speeds of that week. Thus, the term "noisy" is used in the same sense it has been employed thus far, namely to describe levels of seismic rather than wind activity. Although in what follows we will commonly associate particular weeks with a single ground displacement or wind speed (*e.g.*, "7-nm vertical displacement at CNTR on week 20"), it is important to keep in mind that the displacements and speeds mentioned are averages not of the 168 hours making up each week but only of the noisiest hour of each week studied. The horizontal red line in the figure is at 25 nm, the upper limit for acceptable ground displacement at the site. Note that while CNTR and NELG had already started recording by week 7, SWLG and NWLG started recording on weeks 11 and 17, respectively (Table 5.1). The gaps in the displacement plots of SWLG and NWLG postdating their installation indicate times during which the stations were down.

The first features that jump out in most plots of Figure 5.2 are the

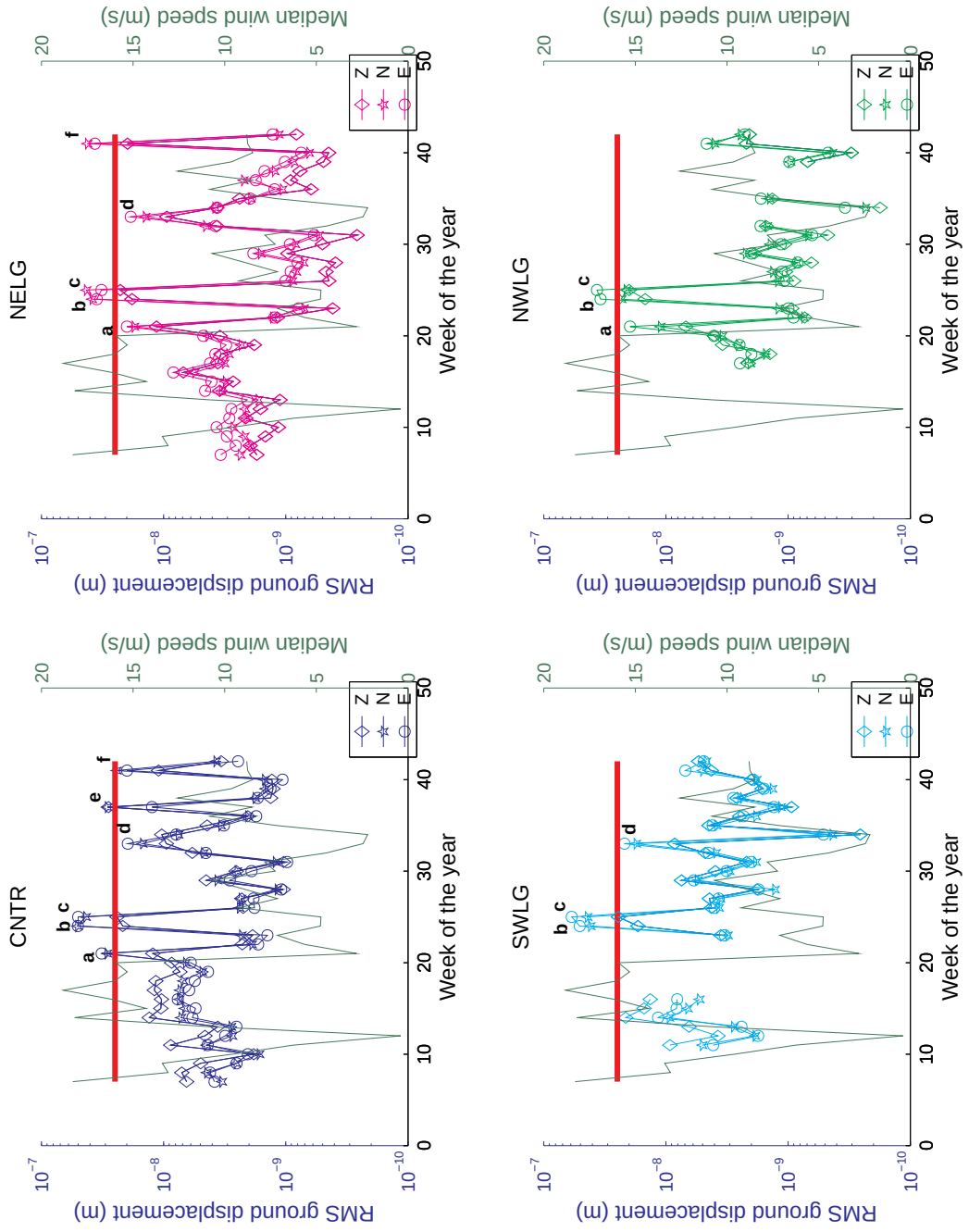

Figure 5.2: RMS ground displacements and wind speeds (solid line) for the noisiest hour of each week between February and October 2003. The horizontal bar is at 25 nm.

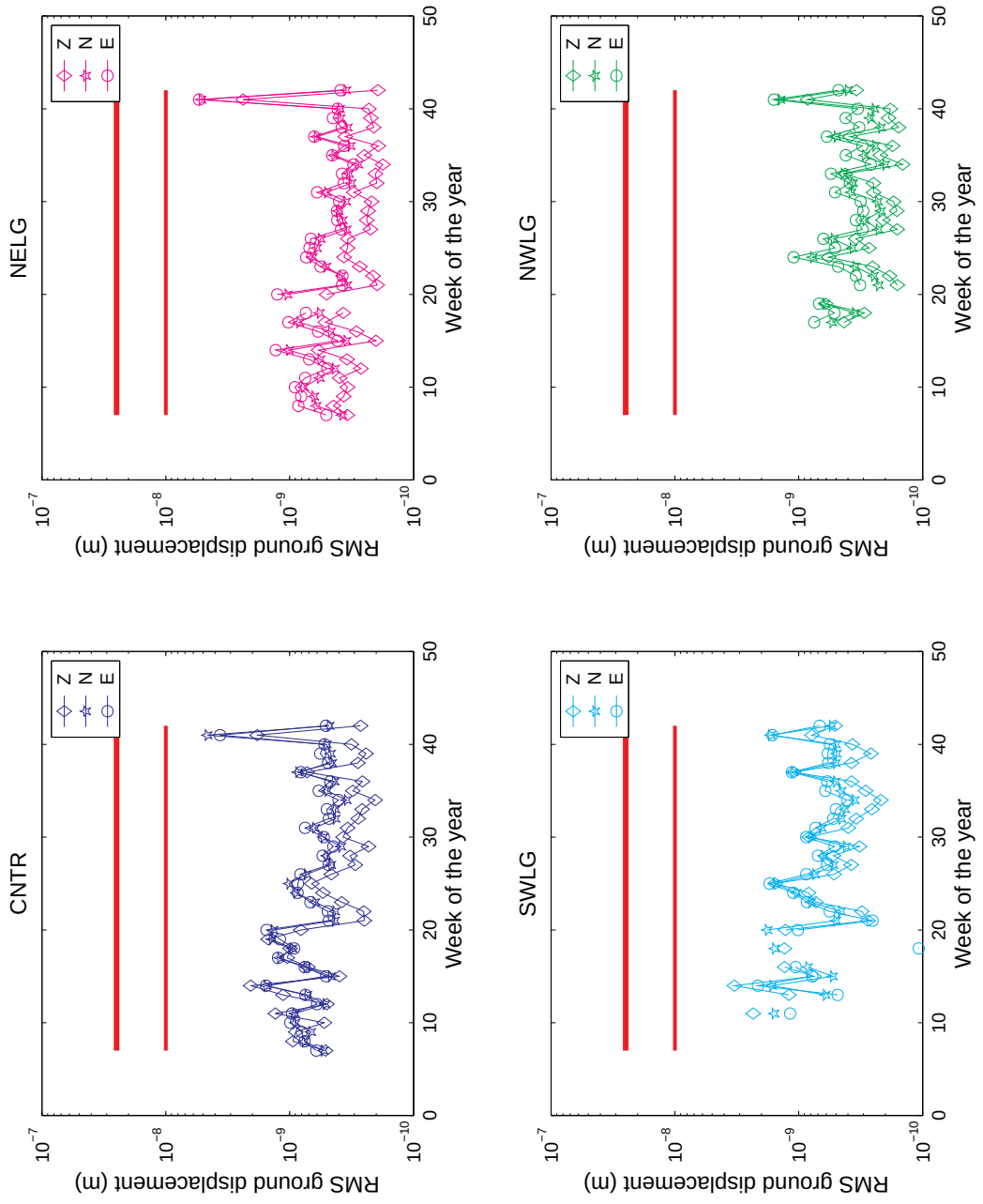

Figure 5.3: RMS ground displacements for the median noise hour of each week between February and October 2003. The horizontal bars are, from top to bottom, at 25 and 10 nm, respectively. Note that there is somewhat of a correlation between the windiest season of the year (Fig. 5.2) and the median noise hours for the corresponding weeks. The anomalous peak in week 41 was caused by the crew performing the geotechnical survey of the MRO site.

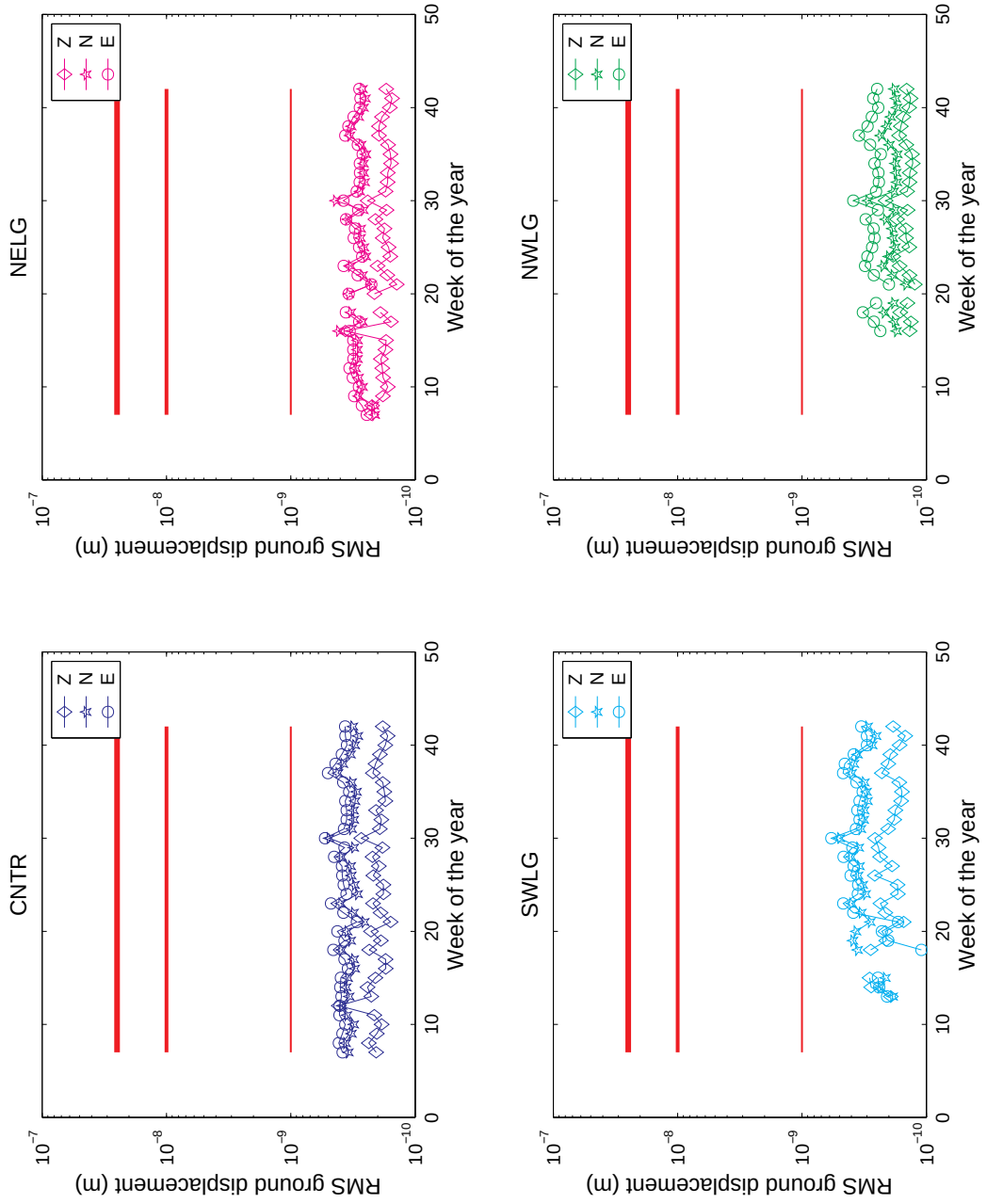

Figure 5.4: RMS ground displacements for the quietest noise hour of each week between February and October 2003. The horizontal bars are, from top to bottom, at 25, 10 and 1 nm, respectively.

peaks in ground displacement, labeled **a** through **f**, in weeks 21, 24, 25, 33, 37 (CNTR only), and 41. These peaks correspond to the double-digit displacements that jump out of Table 5.2 in the rows corresponding to those six weeks, and are anomalous in the sense that they are not a consequence of the continuous background noise at the site but are caused by relatively long- to short-duration transients with amplitudes large enough to effectively bias the hourly ground displacement averages, as will be discussed in more detail in what follows. Although not necessarily free of minor transients, ground displacements corresponding to weeks other than these six weeks are representative of the typical displacements that can be observed at the MRO site as a consequence of continuous background noise.

It is evident from the figure that a good correlation between wind activity and seismic noise at the site is observed only during the windiest period of the year (weeks 14 through 20), when wind speeds regularly exceed 15 m/s. Curiously enough, CNTR and SWLG stations are observed to be more sensitive to wind-generated noise, which is believed to couple to the ground mainly through the roots of swaying trees, than NELG station, which is much closer to the treeline on Magdalena Ridge. In particular, the vertical components of CNTR and SWLG are observed to be more sensitive to wind-generated noise than any other components in the seismic array; however, while the component of CNTR that is second most sensitive to such noise is the north-south component, in SWLG the second most sensitive component is the east-west. These differences in inter-station component sensitivity suggest that the seismic excitation mechanism triggered by the wind is not exactly the same at all four station sites. While minor differences in sensitivity from station to station could

Figure 5.5: Topography at the deployment site of SWLG (looking north). Note the 8° to 10° slope that facilitates the coupling of wind-generated noise to the ground. (Photo courtesy of AMEC.)

have a purely instrumental origin (i.e., small deviations from the manufacturer-advertised sensitivity of 1500 mV/(mm/s) in each seismometer delivered), the fact that the relative component sensitivities are not the same (i.e., the vertical component is not the most sensitive to wind in *all* stations) suggests that these differences in sensitivity to wind-generated noise are probably related to minor differences in vault construction and in topography around each station. (Recall that in Chapter 2 we discarded differences in shallow geology as possible sources of differences in seismic response from station to station.) In fact, the recording of the largest wind-triggered ground displacements by SWLG's vertical component (weeks 14 through 16) can be explained by the station's location relative to incoming winds during these times: on weeks 14 through 16 winds blew across Magdalena Ridge preferentially from the west and southwest (Appendix D). With SWLG station installed on an 8°- to 10°-dipping slope (Fig. 5.5) that eventually steepens into a cliff that defines the western slope of Magdalena Ridge, strong (> 15 m/s) winds blowing into the site from the west were able to impinge directly on the sloping terrain hosting the station and build a pressure field most strongly sensed by the vertical component of the seismometer without the assistance of any trees. CNTR station, not far away from the western cliff, but installed on flat rather than west-dipping terrain, is also affected by winds blowing in from the west and southwest, but not as much as SWLG; vertical displacements at SWLG and CNTR were observed to be as large as 22 and 14 nm, respectively. NELG, on the other hand, located at the opposite (i.e., east) end of Magdalena Ridge, is comparatively well-shielded from these winds, and thus does not exhibit ground displacements larger than 10 nm during the windiest period of the year (weeks 14 through 20). NWLG,

operational during the later half of the windiest season and as close to the western cliff as SWLG, mysteriously records displacements of under 5 nm during this period.

The correlation between ground displacement and wind speed at the MRO site during seasons other than the windiest season of the year is not as strong. It could be argued that on weeks 7 through 13, just prior to the windiest season, the fact that the vertical components of ground motion at CNTR and SWLG are largest and the fact that winds are blowing in roughly from the west throughout this time (two patterns that are also observed during the windiest season), should suggest that the major source of seismic background noise during weeks 7 through 13 is also wind-to-ground coupling. Although this seems to hold true at all three stations that were operational during this period (with the east-west rather than the vertical component dominating in NELG), at one such station (CNTR) the case seems to break in week 10, when winds averaging $\sim$6 m/s are associated with ground displacements as large as those in the previous three weeks, which were accompanied by winds twice as strong ($\sim$12 m/s). Moreover, the motion sensed by the vertical component of CNTR was about the same in both weeks 12 and 13 ($\sim$4 nm), and even though the wind in both weeks was observed to come from the same direction (northwest), while the wind speed is moderately strong on week 13 ($\sim$10 m/s), it is next to zero on week 12. Thus, vertical-component dominance is not always a reliable indicator of wind-generated seismic noise at the site.

Visualizing the strength or weakness of the correlation between ground displacement and wind speed in the weeks after the windiest season of the year

is made difficult by the noise spikes (> 10 nm) produced by transient phenomena (see next section). Noise spikes aside, however, it is evident that in weeks 21 through 42 ground displacements at all stations are, on average, smaller relative to those in weeks 7 through 20, and correlate reasonably well with the lower wind speeds observed later in the year. The correlation is not strong, however, as the weeks on which major peaks and valleys in wind speed are observed during this later period of the year do not always correspond to the weeks on which major (transient-unrelated) peaks and valleys in ground displacements are observed.

To summarize, the relationship between wind and background noise at the MRO site is two-fold and quite clear when transient-related noise spikes are excluded from the analysis: during the first part of the study period (weeks 7 through 20), which includes the windiest season of the year (weeks 14 through 20), wind speeds observed during the hours of maximum seismic noise average ∼13 m/s and are the likely cause of the observed ground displacements larger than 10 nm. CNTR and SWLG seem to be more sensitive during this earlier part of the year because of their locations on Magdalena Ridge relative to the incoming winds, all of which are observed to arrive within 60 degrees of west. In fact, Klinglesmith *et al.* (manuscript in preparation, 2004) show that the only large peak in a histogram of wind direction based upon data recorded at MRO between 2000 and 2004 was centered at approximately west-southwest. During the second part of our study period (weeks 21 through 42), wind speeds during the hours of maximum seismic noise averaged ∼7 m/s and correlate reasonably well with the lower ground displacements observed at all stations during this period. For example, both vertical and horizontal

ground displacements at CNTR during this period did not exceed, on average, 4 nm, while during the first period discussed (which includes the windiest season), vertical and horizontal ground displacements at this station averaged 9 and 6 nm, respectively. Although the second period of the year (weeks 21 through 42) features lower wind speeds showing no preferential direction, this period features New Mexico's monsoon season (July and August), when most of the year's rain falls during early-evening thunderstorms every other day or so. In fact, some of the noisiest hours of the week during this period may have reached such status as a result of lightning striking near the MRO site. Nevertheless, the bottom line is again good news: even when wind speeds are highest ($\sim$18 m/s), ground displacements at the most wind-sensitive station locations (SWLG and CNTR) do not exceed 25 nm. Moreover, *differential* ground displacements (Table 5.5) during these times of increased wind activity between weeks 14 and 20 were observed to get close to or exceed 25 nm on only one occasion (week 14). During the noisiest hour of this week, two of the three vertical differential displacements involving the most wind-sensitive station (SWLG) were measured to be 22 and 26 nm. Note, however, that under the drastic and unlikely assumptions of coherent motion exactly out of phase, vertical ground displacements could be as large as 36 nm if the site is subject to such strong wind speeds (*e.g.*, SWLG relative to CNTR in week 14 of Table 5.2). Nevertheless, it is clear from the PSD plots for the characteristic noise periods of each week in the eight-month study period (Appendix B) that motion between stations is generally incoherent except within the oceanic microseism band, between about 0.1 and 0.7 Hz.

5.1.4 Sources of anomalous noise peaks

Ground displacements in Figure 5.2 near or beyond the 25-nm upper limit of acceptable motion are labeled **a** through **f** in the plots and were all caused by transient phenomena rather than by continuous background noise, as inferred from the corresponding velocity seismograms. All transient phenomena below listed are analyzed in more detail in the following section. Most such phenomena were related to earthquakes, whether local, regional, or long-distance ones. The earthquake magnitude scales mentioned herein are all logarithmic measures of the "size" of the earthquake but are only roughly equivalent to each other, since they are estimated using different earthquake parameters: duration magnitude (M_d) is estimated from the duration of earthquake vibrations and is suitable only for local events (subsection 5.2.1); body-wave magnitude (m_b) is estimated from the largest amplitude of the body-wave train (usually a P-wave very early in the seismogram record) and is suitable for characterizing global events; moment magnitude (M_W) is computed from the physical parameters of the earthquake (the area of the fault, average slip, and shear modulus of the rock) and is also suitable for global events.

a– Week 21 (Sunday, May 25, 6:00-7:00 pm MST): three local earthquakes, all lasting less than ∼30 s (as sensed at MRO), with a gap of ∼24 min between the first and second earthquakes and a gap of just 4 min between the second and third one. Since duration magnitudes are simply computed from $M_d = 2.79 \log_{10} T_d - 3.63$ (where T_d is the duration of the earthquake in seconds), these three local earthquakes had a magnitude of less than ∼0.5. (However, in the more detailed analysis of local earthquakes of subsection 5.2.1

we refer to catalogs of local earthquakes in which event magnitudes were determined based on event durations as recorded at stations *within* the Socorro Seismic Anomaly; therein the above three local earthquakes would have been cataloged as having duration magnitude 1.3 or so.)

b− Week 24 (Monday, June 16, 6:00-7:00 am MST): two local earthquakes lasting ∼30 s and ∼60 s (as sensed at MRO), respectively, within a 26-min interval; truck driving along Langmuir Road toward Langmuir Lab (Fig. 2.3); the maximum amplitudes recorded due to the truck are comparable to the maximum amplitudes of the longer earthquake. The two earthquakes would have been cataloged in a hypothetical "MRO earthquake catalog" as having duration magnitudes of about 0.5 and 1.3, respectively. (However, in the existing catalog based on their duration at seismic stations within the Socorro Seismic Anomaly they must have been cataloged, if they were considered large enough to be of interest, as having duration magnitudes of about 1.3 and 2.2, respectively.)

c− Week 25 (Friday, June 20, 12:00-1:00 am MST): deep, large-magnitude earthquake with epicenter in the Amazon (M_W 7.1), the waves of which started arriving at MRO at approximately 12:28 am and continued to arrive past the end of this 1-hour time window identified as the noisiest hour of the week.

d− Week 33 (Friday, August 15, 2:00-3:00 am MST): two intermediate-magnitude shallow earthquakes with epicenters in the Gulf of California (m_b 4.9) and off the coast of northern California (M_W 5.3), respectively. While the earlier earthquake (northern California) had a duration of ∼15 min at MRO

(2:26 to 2:41 am), its maximum wave amplitudes were roughly six times smaller than those associated with the later earthquake (Baja California), which had approximately the same duration at MRO (2:46 to 3:00 am). The most prominent waves from the earlier event were 10-s-period surface waves[7] recorded in the 5-min interval between 2:33 and 2:38 am, approximately; the most prominent waves of the later event were, curiously enough, shorter-period waves recorded in the 7-min interval between 2:46 and 2:52 am, approximately.

e– Week 37, CNTR only (Thursday, September 11, 7:00-8:00 am MST): during this early working-day hour, the AMEC crew assigned to perform the geotechnical survey at MRO (Chapter 2) was getting its machinery ready to drill a 35-ft deep borehole right next to CNTR.

f– Week 41, CNTR and NELG mostly (Thursday, October 9, 7:00-8:00 am MST): AMEC machinery and trucks driving by the seismic stations caused the unusually high ground displacements recorded during this early working-day hour.

5.2 Transients

To investigate in more detail the effect of finite-duration phenomena on ground motion at the site, we investigated examples of each of the types of transients observed earlier when analyzing the noisiest night-time hours of

[7]Surface waves with periods of about 20 s (rather than 10 s) are typically the most prominent waves from distant shallow earthquakes that are recorded on seismograms. Moreover, note that at all three stations recording this event (Figure 5.2), vertical displacements are not as large as horizontal displacements. This is a reasonable observation because of the two main types of surface waves, namely Rayleigh waves and Love waves, only Rayleigh waves can be detected by the vertical component of a seismometer.

the entire study period. However, the following examples were not necessarily picked from the night-time hours, as the associated transients may occur at any time.

5.2.1 Local earthquakes

"Local" earthquakes are typically considered to be those whose epicenter is fewer than 100 km away from the observation point. In the case of the MRO site, most local earthquakes are related to the Socorro mid-crustal magma body (Fig. 2.1), an extensive and relatively flat body of molten rock with an upper surface area of at least 3400 km^2, residing at about 19 km underneath the Socorro area of the Rio Grande rift (Balch *et al.*, 1997). Because of the unusually high earthquake activity in the area, compared to the rest of New Mexico, the area is referred to as the Socorro Seismic Anomaly (SSA). The earthquakes thought to be generated by the slowly-inflating Socorro magma body are shallow events (between about 2 and 10 km deep) and are typically low-magnitude earthquakes ($M_d < 2.0$), also referred to as microearthquakes. These relatively weak events occur rather frequently, having recurrence intervals in the order of days to weeks, and often occur in "swarms", that is, prolonged sequences of earthquakes closely related in time and space. A microearthquake swarm in the SSA can consist of a few tens of small earthquakes and can last for as long as several weeks. Decades of swarm observations in the SSA indicate that swarms are not precursors to larger events. Although stronger events (M_d $2.0 - 5.8$) have been recorded in the area (Sanford *et al.*, 2002), their recurrence intervals are much longer, the strongest ones being recorded every few years or decades.

The local earthquake analyzed in this study (M_d 1.07) had its epicen-

ter near the town of Lemitar, just 8 km north of Socorro (Fig. 2.1). The event had a duration of about 30 s at the MRO site (just outside the SSA) and of 49 s, on average, at the eight stations located within or approximately within the SSA, all operated by the New Mexico Tech Geophysics Program. However, the earthquake was too small to show above noise levels at the seven stations in southeast New Mexico also operated by New Mexico Tech. Despite its small magnitude, the Lemitar earthquake caused RMS ground displacements of up to 34 nm (22 nm per component, on average), as shown in Table 5.7, and differential RMS ground displacements of up to 39 nm (28 nm per component pair, on average), as shown in Table 5.8, over the 30 s of its duration. The largest displacements by far were observed in the horizontal components of CNTR, while the largest differential displacements were observed to be those of the horizontal components of CNTR relative to those of NELG. However, local earthquakes such as this one are such short-duration events that they do not bias the RMS ground displacement when the average is taken oven a full hour. This is why none of the major peaks in maximum RMS ground displacement of Figure 5.2 is caused by an isolated local earthquake. Nevertheless, we have already seen that on two occasions (Fig. 5.2: weeks 21 and 24) *swarms* of three or more local earthquakes were capable of biasing hourly RMS ground displacements beyond the 25-nm upper limit for acceptable motion during our 36-week study period. Thus, assuming that 2003 was a typical year in terms of local earthquake activity, we can expect that during any future 52-week period interferometry will be compromised by 3 or so swarms of local earthquakes.

We can make an even more rigorous estimate of the downtime due to local earthquakes by focusing not on hourly RMS averages but on very short-

period peaks. Recall that optical pathlengths (section 1.4) must be stable to within 25 to 100 nm (depending on wavelength) during the 10 to 100 ms that a typical fringe measurement lasts. Also note that, given the small fringe measurement periods, local earthquakes would have to trigger seismic waves with frequencies of at least 10 Hz (and, of course, amplitudes of at least 25 nm) in order for them to pose a problem for interferometry. Because the M_d 1.07 ($\sim$50-s-long) local earthquake above described resulted in ground displacements at MRO that were just a few nm above acceptable, it is reasonable to assume that the operation of the interferometer will not be compromised by weaker earthquakes (i.e., those with magnitude less than 1 or, equivalently, shorter than 60 s in duration). It is clear from the power spectral density plots of the minute-long earthquakes recorded in this study (*e.g.*, Appendix B: highest noise periods of weeks 21 and 24; see subsection 5.1.4 for an explanation) that although they exhibit a peak between 1 and 2 Hz they still have considerable power around 10 Hz and thus are capable of affecting fringe measurements lasting a few tens of milliseconds or so. The question then becomes: How many local earthquakes (i.e., SSA events) with magnitude 1 or greater can be expected during a particular time period (one year, say) at MRO? It can be inferred from annual recurrence relations in the SSA for the time period 1962-1998 (Fig. 5.6) that approximately 30 or so local earthquakes with magnitude 1 or greater can be expected to occur in any given year. Assuming that these earthquakes are as likely to occur during the daytime as during the night-time, we expect 15 or so local earthquakes (each at most a few minutes in duration) to cause problems for fringe measurements in any given year.

RMS ground displacement (nm)

Station component		Above 1 Hz	Above 2 Hz	Above 5 Hz
CNTR	N	34	31	20
NWLG	N	19	16	11
NELG	N	23	20	11
SWLG	N	25	19	10
CNTR	E	34	29	21
NWLG	E	21	17	6
NELG	E	26	23	11
SWLG	E	25	21	14
CNTR	Z	17	15	11
NWLG	Z	11	9	6
NELG	Z	15	13	7
SWLG	Z	13	12	7

Table 5.7: RMS ground displacements, rounded up to the nearest nm, due to the 30-s-long Lemitar earthquake (M_d 1.07) that originated approximately 35 km east of the MRO site. Note that the reduction of noise between the Above-1-Hz noise range and the Above-5-Hz range can be greater than 50%, *e.g.*, from 23 to 11 nm in the north-south component of NELG. This is an indication that seismic noise due to this local earthquake has its peak somewhere between 1 and 5 Hz.

Differential RMS ground displacement (nm)

Station component		Above 1 Hz	Above 2 Hz	Above 5 Hz
CNTR-NWLG	N	37	35	25
CNTR-NELG	N	39	36	24
CNTR-SWLG	N	33	31	20
NWLG-NELG	N	26	24	15
NWLG-SWLG	N	31	26	17
NELG-SWLG	N	35	29	16
CNTR-NWLG	E	35	32	21
CNTR-NELG	E	38	36	24
CNTR-SWLG	E	37	34	21
NWLG-NELG	E	28	25	13
NWLG-SWLG	E	31	27	14
NELG-SWLG	E	36	32	17
CNTR-NWLG	Z	16	15	11
CNTR-NELG	Z	18	18	12
CNTR-SWLG	Z	16	16	12
NWLG-NELG	Z	16	15	8
NWLG-SWLG	Z	16	14	8
NELG-SWLG	Z	19	18	9

Table 5.8: Differential RMS ground displacements, rounded up to the nearest nm, due to the 30-s-long Lemitar earthquake (M_d 1.07) that originated approximately 35 km east of the MRO site. Note once more that the reduction of noise between the Above-1-Hz and the Above-5-Hz noise ranges can be larger than 50%, *e.g.*, from 19 to 9 nm in the vertical component of NELG relative to that of SWLG.

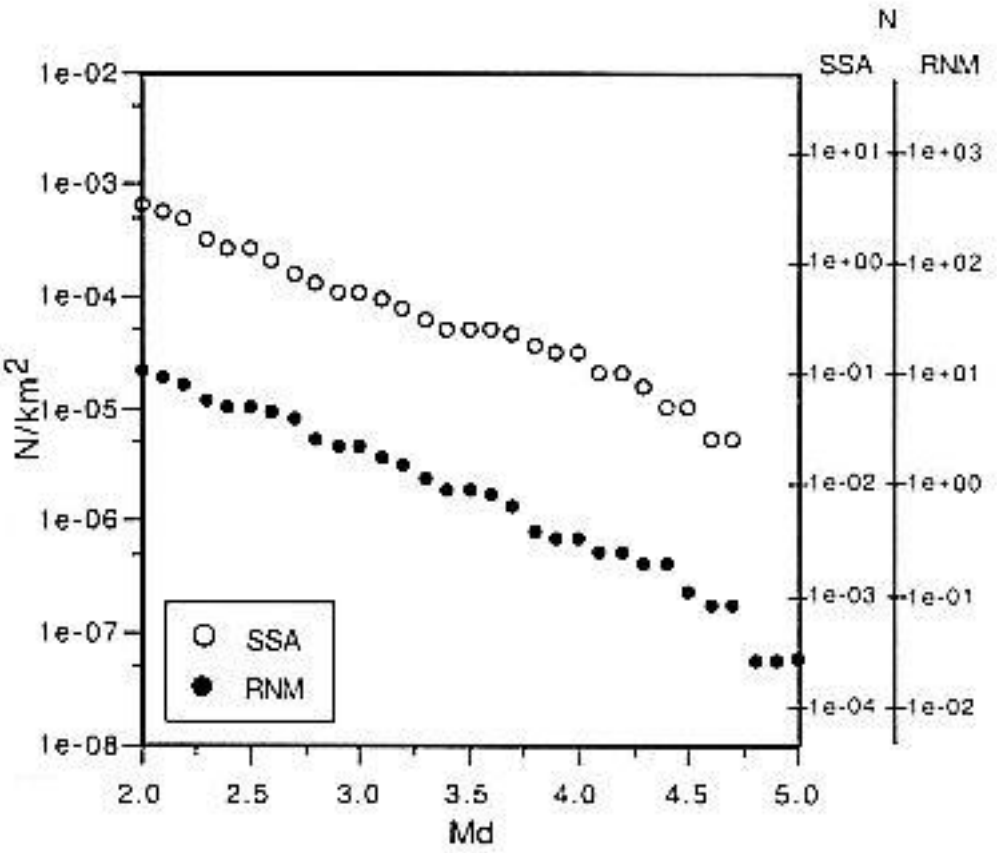

Figure 5.6: Annual recurrence relations for the Socorro Seismic Anomaly (SSA) and the rest of New Mexico (RNM) and bordering areas for the time period 1962-1998. The catalog contains 473 events, 125 of which are within the SSA. Although the data are complete only for earthquakes larger than magnitude 2.0, it can be inferred that ∼30 SSA earthquakes with magnitude equal to or greater than 1.0 can be expected to occur in any given year. (From Lin, 1999.)

5.2.2 Regional earthquakes

"Regional" earthquakes are typically considered to be those whose epicenter is between 100 and 1400 km from the point of observation. If we relax this definition we can regard as regional earthquakes those whose epicenter occurs within the North American continent or just off its coasts. Most regional earthquakes with magnitudes large enough to be a cause of concern for interferometry at MRO are related to the Pacific-North American boundary zone, which extends more or less along the coast of North America, from the southernmost tip of Baja California to the Aleutian Islands off the coast of Alaska. While seismic activity in the southern part of the boundary is triggered by the opening of the Gulf of California by sea-floor spreading and does not cause noteworthy earthquakes, seismic activity further north is related to the San Andreas fault system (in essence a transform fault) and by the subduction of the Pacific plate beneath the North American plate just off the coast of Alaska, both of which have been responsible for triggering large and destructive earthquakes roughly every decade or so (Northridge, CA, 1994; Landers, CA, 1992; Loma Prieta, CA, 1989; San Fernando, CA, 1971; Alaska, 1964). On the other hand, New Mexico and adjacent states are in comparison very seismically quiet regions. Similarly, because it is far away from plate boundaries, the remaining continental United States is devoid of large earthquake activity, although a few notable intraplate earthquakes have occurred since the early nineteenth century (Hebgen Lake, MT, 1959; Charleston, SC, 1886; New Madrid, MO, 1811-1812).

The regional earthquake recorded during the data acquisition period

this study and that was responsible for nearly unacceptable ground displacement during the noisiest hour of week 33 (Fig. 5.2) was a shallow (∼10-km-depth), moderately strong event (m_b 4.9) with epicenter in the Gulf of California, about 864 km from the MRO site. Although the noisiest hour of this week also featured another moderately strong earthquake (section 5.1.4), the epicenter of this other earthquake was twice as far away from MRO as that of the Baja California earthquake, so despite its larger magnitude (M_W 5.3) the amplitudes of its most prominent waves were observed to be roughly six times smaller at MRO. Moreover, since this less prominent earthquake did not last longer than the Baja California earthquake, it is reasonable to assume that the Baja California earthquake is solely responsible for the bias in ground displacement during the noisiest hour of week 33. Although the Baja California earthquake had a duration of just 15 min or so (2:46 to 3:00 am), the RMS ground displacements during the hour from 2:00 am to 3:00 am rose 100% from their typical average of 7 or 8 nm (subsection 5.1.1) to an average of 15 or 16 nm, with the maximum displacement being observed at the east-west component of SWLG, namely 22 nm (Table 5.2: week 33). On the other hand, differential ground displacements were skewed by an insignificant amount, from their typical average of 9 or 10 nm (subsection 5.1.2) to an average of 11 nm, with the maximum differential displacement being that of the east-west component of SWLG relative to that of NELG, namely 22 nm (Table 5.5: week 33). In other words, Baja California earthquakes of this nature, as well as distant earthquakes in general, cause the seismic stations at MRO to move fairly coherently. However, a slightly stronger earthquake with otherwise similar characteristics and with epicenter in the same location would have resulted

in differential ground displacements larger than acceptable.

To address the important issue of regional earthquake recurrence, we performed a search of moderately strong to strong regional earthquakes (magnitude 4.9 or larger in any magnitude scale: m_b, M_W, etc.) that occurred within the last 30 years (1974-2003) in a 1400 km-radius centered about MRO. The search, based on the Preliminary Determination of Epicenters (PDE) catalog at the website of the National Earthquake Information Center (http://neic.usgs.gov), produced 597 earthquakes, and thus a yearly average of nearly 20 earthquakes. Assuming that these earthquakes are as likely to occur during the daytime as during the night-time, we expect 10 or so regional earthquakes (magnitude 5 or larger) to cause trouble for interferometry on any given year. Furthermore, assuming that the strongest of these earthquakes cause unacceptable ground displacement for up to one hour, the operational downtime of the interferometer due to regional earthquakes will be at most 10 hours a year.

Note that earthquakes weaker than magnitude 5 were not considered for this simple statistical computation because they were not the cause of any of the noise peaks in the 36 weeks of 2003 studied. And although earthquakes somewhat weaker than magnitude 5 but *closer* to MRO (*e.g.*, with epicenter in New Mexico or adjacent states) could certainly have an impact on ground motion comparable to that of stronger earthquakes with epicenters further away, earthquakes in New Mexico and adjacent states are typically much weaker than magnitude 5 (Lin, 1999, Appendix II): out of the 710 events with magnitudes 2.0 and above recorded in New Mexico and bordering areas (excluding the

SSA, which is a source of local rather than regional earthquakes) between 1962 and 1998, only 18 earthquakes had moderate magnitudes (i.e., between 4.0 and 5.0), thus giving an average of just one moderately-strong earthquake every two years. None of the 710 earthquakes recorded in this 37-year period had a magnitude larger than 5.0; 140 earthquakes had magnitudes between 3.0 and 3.9, and the remaining 552 events ($\sim$ 78% of all events recorded) had magnitudes between 2.0 and 2.9. Further, note that because magnitude scales are logarithmic, a decrease in one unit, as from magnitude 5.0 to magnitude 4.0, represents a ten-fold decrease in seismic wave amplitude. Thus, a magnitude-5.0 earthquake is a hundred times stronger than a 3.0-earthquake and a thousand times stronger than a 2.0-earthquake.

5.2.3 Long-distance earthquakes (teleseisms)

"Teleseisms" or long-distance earthquakes are typically considered to be those whose epicenter is more than 1400 km away from the observation point. Just like with local and regional earthquakes, for which we respectively singled out the SSA and the Pacific-North American boundary zone as major sources, it is also possible to single out major sources of long-distance earthquakes despite the fact that earthquakes occur everywhere in the Earth's crust. Because seismic waves are attenuated as they radiate from their source, a teleseism must evidently be strong enough for its energy to cause trouble at MRO after traveling a very long distance from its epicenter, and thus in this study we need only be concerned about the strongest teleseisms. Moreover, it is well-known that most of the world's moderately-strong to strong earthquakes ($m_b >$ 5) occur at the boundaries of tectonic plates (namely, the fifteen or so rigid sec-

tions into which the earth's lithosphere is broken up) and that the largest of these earthquakes occur along subduction zones (namely, regions along which an oceanic plate sinks beneath a continental plate). The world's most prominent subduction zones are located in the Circum-Pacific belt, an area of high seismic activity along the coast of roughly all continents bathed by the Pacific Ocean: Oceania (notably New Zealand and Papua New Guinea), Asia (notably Indonesia, Philippines, and Japan), North America (except most of the west coasts of the United States and of northern Mexico, where transform and ridge portions dominate throughout the length of the Pacific-North American plate boundary), and the west coasts of Central and South America.

The teleseism recorded during the data acquisition stage of this study and that resulted in unacceptable ground displacement during the noisiest night-time hour of week 25 (Fig. 5.2) was a large (M_W 7.1), 558-km-deep earthquake with epicenter in the Amazon Jungle, near the border between Peru and Brazil, some 5920 km from MRO. The event had a duration of approximately one hour (12:28 to 1:30 am, with most of the energy being received in the first half hour) and, despite its distant epicenter, it caused ground motion during the hour from 12:00 to 1:00 am to rise dramatically: RMS ground displacements rose nearly 500% from their typical average of 7 or 8 nm to an average of 35 or 36 nm, with the maximum displacement being observed at the east-west component of SWLG, namely 60 nm (Table 5.2: week 25); similarly, differential ground displacements were skewed by a large amount from their typical average of 9 or 10 nm to an average of 32 nm ($\sim$7 nm beyond acceptable), with the maximum differential displacement being that of the east-west component of SWLG relative to that of NWLG, namely 71 nm (Table 5.5:

week 25). However, differential displacements between corresponding station components were, on average, smaller than the individual station displacements recorded during the transient event, which indicates that the Amazon Jungle earthquake, just like the Baja California earthquake, caused the seismic stations at MRO to move fairly coherently. Note that a slightly weaker earthquake (say, M_W 6.3 or 6.4), would have probably still caused some differential displacements to be just beyond the 25-nm upper bound for acceptable ground motion.

To address the important issue of teleseism recurrence and, thus, to estimate the operational downtime of the interferometer due to teleseisms, it would be ideal to be able to predict the amplitudes of ground displacement observed at MRO due to any given earthquake as a function of epicentral distance from the interferometer site. In other words, it would be ideal to establish what magnitude an earthquake with epicenter 1400 km away from MRO should have for it to cause trouble for interferometry, what magnitude it should have if its 3000 km away, if its 5000 km away, and so on. However, such estimates would be subject to numerous uncertainties, since seismic waves from different long-distance earthquakes arrive at MRO along different paths which attenuate the traveling seismic energy to different extents in each particular case. Nevertheless, given that we know that a 6000-km-distant earthquake of magnitude $\sim$7 causes unacceptable ground motion at MRO, we can assume that teleseisms of magnitude 7 or larger with epicenter *anywhere* in the world will cause trouble for interferometry. In making this assumption note that because the effect at MRO of a magnitude-7 earthquake on the exact opposite end of the world may not be large enough to disturb the interferometer, we might in fact be overesti-

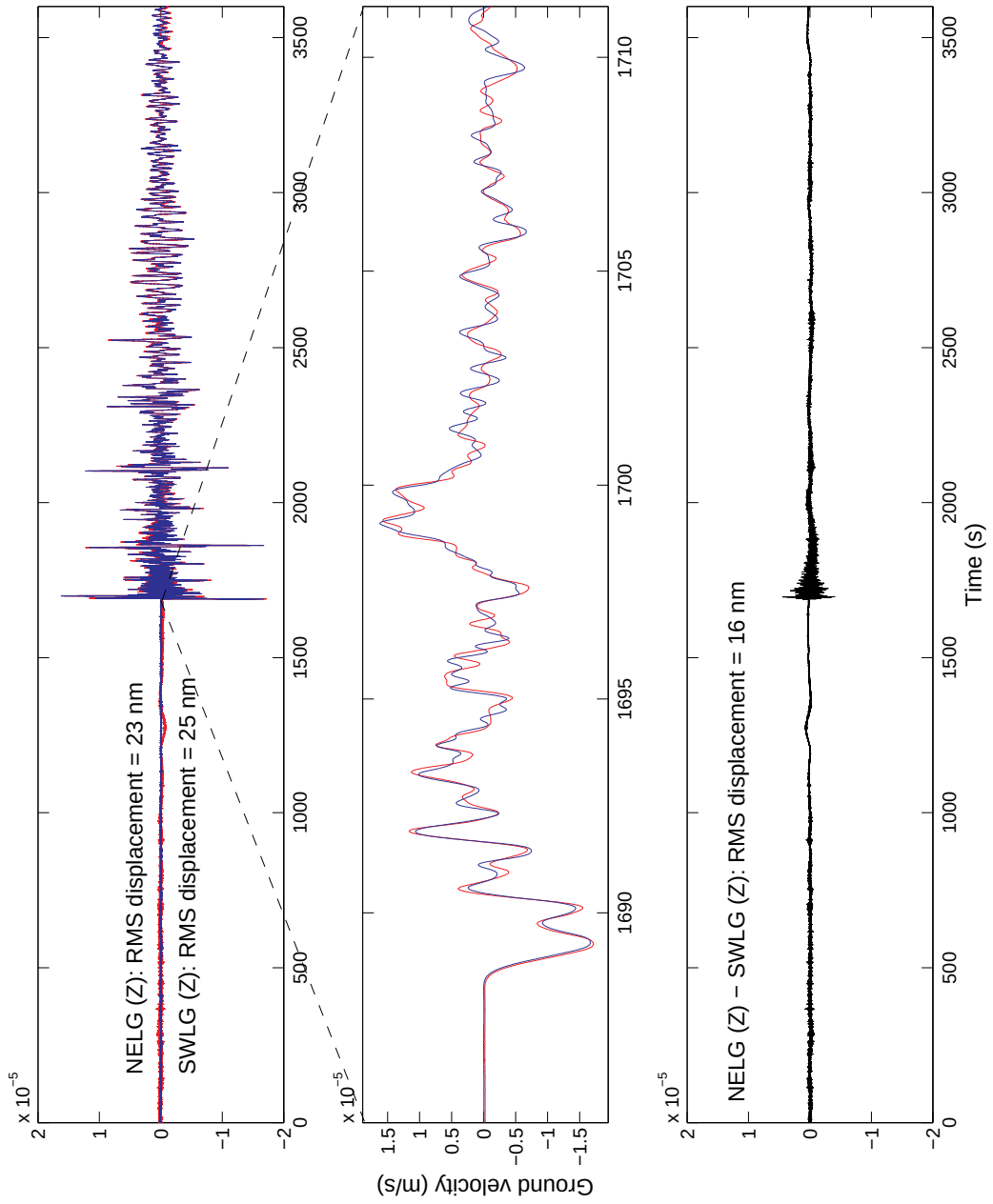

Figure 5.7: *Top*: Seismograms of the deep Amazon earthquake (M_W 7.1) of June 20, 2003, as sensed at MRO: vertical components of NELG (blue) and SWLG (red). *Middle*: Although the seismic energy does not reach both stations simultaneously (the stations are 200 m apart), motion at both sites is still fairly coherent. *Bottom*: The differential 1-hour-long seismogram has an RMS displacement that is smaller than either of the two individual hourly average displacements.

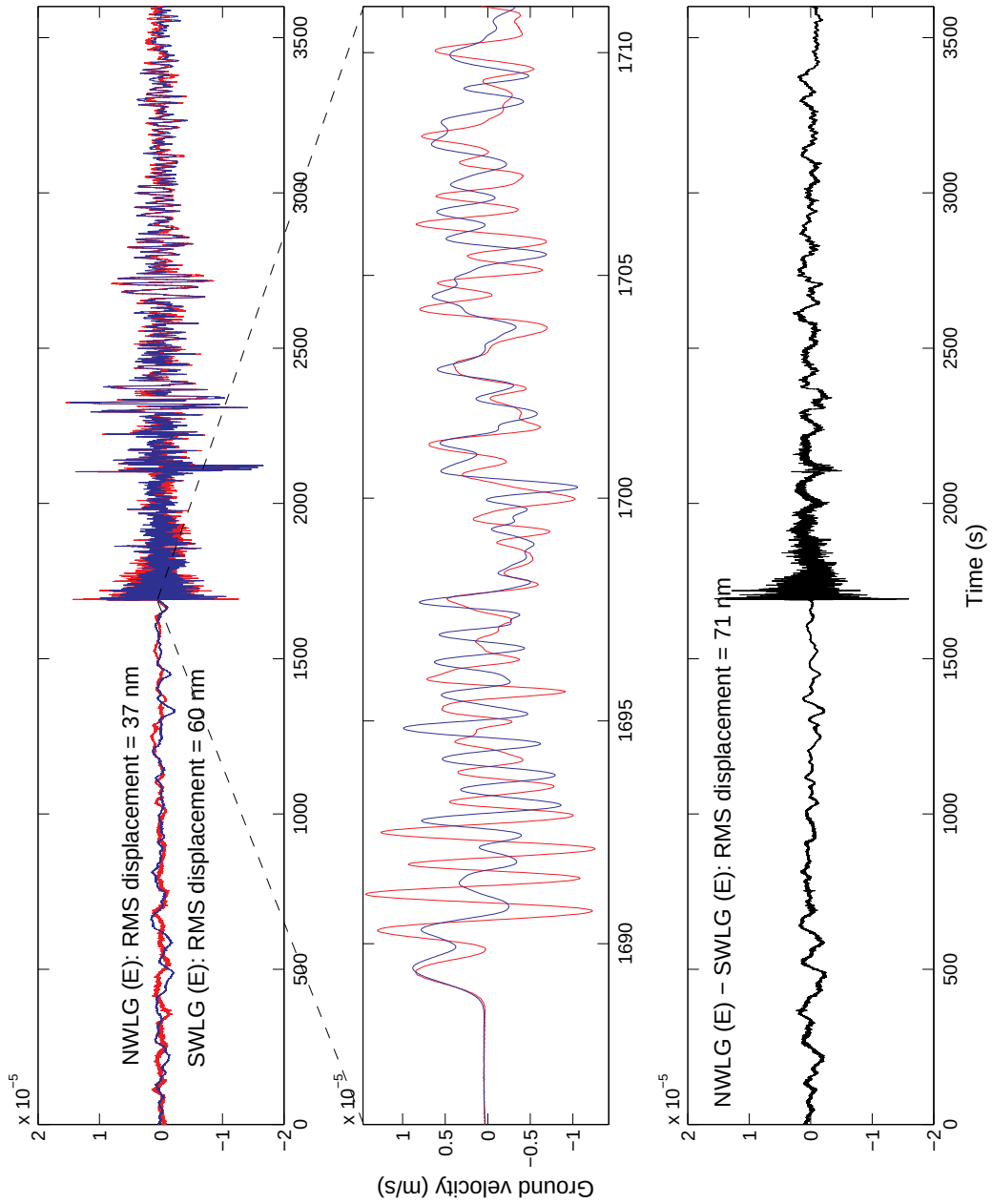

Figure 5.8: *Top*: Seismograms of the deep Amazon earthquake (M_W 7.1) of June 20, 2003, as sensed at MRO: east-west components of NWLG (blue) and SWLG (red). *Middle*: Unlike motion in Fig. 5.7, in this case motion between both sites is incoherent. *Bottom*: The differential 1-hour-long seismogram has an RMS displacement that is *larger* than both of the two individual hourly average displacements. The lack of coherence is probably due to the lack of competent bedrock at the interferometer site (Fig. 2.5 and Fig. 2.6) and to the local topography.

mating the interferometer downtime due to any such teleseisms. However, this overestimation is more or less balanced out by the *underestimation* of the operational downtime due to earthquakes with epicenters between 1400 and 6000 km and magnitude 7 or greater as well as by the underestimation of downtime that results from ignoring the effect on MRO of earthquakes with magnitudes smaller than 7.

We thus performed a search of strong long-distant earthquakes (magnitude 7.0 or larger in any magnitude scale: m_b, M_W, etc.) that occurred within the last 30 years (1974-2003) anywhere in the world. The search, based on the same PDE catalog used to search for regional earthquakes (subsection 5.2.2), produced 440 earthquakes. Excluding the six earthquakes that occurred within 1400 km of MRO (i.e., regional earthquakes already taken into account in the previous subsection), this gives a yearly average of 14 to 15 earthquakes. Assuming that these earthquakes are as likely to occur during the daytime as during the night-time, we expect 7 or 8 strong teleseisms (magnitude 7 or larger) to cause trouble for interferometry on any given year. Furthermore, assuming that the strongest of these earthquakes cause unacceptable ground displacement for up to one hour, the operational downtime of the interferometer due to long-distance earthquakes will be at most 8 hours a year.

5.2.4 Traffic

We have already seen that noise spikes in seismograms caused by traffic along Langmuir Road (Fig. 2.3) can have maximum amplitudes comparable to the maximum amplitudes produced by a small (∼60-s-duration) local earthquake (subsection 5.1.4**b**). Therefore, just like a swarm of three or more small

local earthquakes, a group of three or more traffic spikes should also be capable of biasing the hourly RMS ground displacements at MRO beyond the 25-nm limit of acceptable motion.

Even though it may seem at first that distinguishing traffic spikes from small local earthquakes in seismograms could be difficult (since both have comparable durations and peak amplitudes), traffic spikes from medium-sized trucks driven along Langmuir Road in fact have easily recognizable signatures: Because Langmuir Road is roughly straight and simply crosses the MRO site, a truck signature on a seismogram grows slowly from background noise levels and after a few seconds suddenly starts growing exponentially until it reaches its peak amplitude, from which it also decays exponentially and slowly blends with ambient noise once more; in other words, unlike earthquakes, traffic spikes on seismograms are rather symmetric. Another key to recognizing truck spikes is that, whereas earthquake signals are observed to start impulsively and almost simultaneously at every MRO station, a particular truck spike is not observed to start at the same time in every station. Moreover, because Langmuir Road is not equidistant to every station, the peak amplitude of a truck spike is observed to vary somewhat from station to station.

Although a single 12-s-duration truck spike can cause ground displacements of up to 35 nm and differential ground displacements of up to 40 nm (Tables 5.9 and 5.10), when RMS displacements are computed for the entire hour within which the short-lived spike is observed, the resultant displacements are indistinguishable from those produced by ambient seismic noise. However, a caravan of three or more trucks would certainly be detrimental to the oper-

ation of the interferometer. It is therefore recommended that four-wheel-drive vehicles be parked as far away as possible from the interferometer site upon arriving to South Baldy and that astronomers move about the interferometer area in smaller, much less powerful vehicles such as golf carts. (Although open golf carts would be unsuitable during adverse meteorologic conditions such as thunderstorms or snowstorms, conveniently enough so would astronomical observations.)

5.2.5 Machinery

Although treated here as a transient, machinery such as cooling systems for the telescopes will probably be run more or less continuously as soon as the interferometer is operational. Thanks to Dr. Bill Winn of Langmuir Lab we were able to compute the RMS ground displacements produced at the MRO seismic array by a 150-kW generator run by a V12 Detroit Diesel engine at Langmuir Lab (Fig. 2.3), approximately 600 m from the center of the array (Tables 5.11 and 5.12). During the one-hour period in which the generator ran, RMS ground displacements sensed by the twelve station components were, on average, between 2 and 3 nm, with the maximum displacement being sensed by the east-west component of CNTR ($\sim$ 6 nm); RMS differential ground displacements were, on average, between 3 and 4 nm, with the maximum differential displacement being that of the east-west component of CNTR relative to that of NELG ($\sim$6 nm, which is the same as the maximum displacement of CNTR by itself). Thus, we observe that when placed $\sim$600 m away from the center of the array (i.e., approximately 800 m from NWLG, 600 m from CNTR and NELG, and 200 m from SWLG), this particular generator produces ground

RMS ground displacement (nm)

Station component		Above 1 Hz	Above 2 Hz	Above 5 Hz
CNTR	N	15	15	15
NWLG	N	1	1	1
NELG	N	34	34	34
SWLG	N	3	3	3
CNTR	E	15	15	15
NWLG	E	1	1	1
NELG	E	35	35	35
SWLG	E	4	4	4
CNTR	Z	12	12	12
NWLG	Z	1	1	1
NELG	Z	10	10	10
SWLG	Z	2	2	2

Table 5.9: RMS ground displacements, rounded up to the nearest nm, due to a 12-s noise spike produced by a medium-sized truck being driven along Langmuir Road on July 7, 2003. The fact that the three displacement columns are nearly identical indicates that the truck noise signal has little power between 1 and 5 Hz and that most of its power ($>$ 1 Hz) is between 5 and 40 Hz, where 40 Hz is the upper limit of sensitivity of the seismometers used in this study.

Differential RMS ground displacement (nm)

Station component		Above 1 Hz	Above 2 Hz	Above 5 Hz
CNTR-NWLG	N	15	15	15
CNTR-NELG	N	38	38	38
CNTR-SWLG	N	16	16	16
NWLG-NELG	N	34	34	34
NWLG-SWLG	N	3	3	3
NELG-SWLG	N	34	34	34
CNTR-NWLG	E	15	15	15
CNTR-NELG	E	40	40	40
CNTR-SWLG	E	15	15	14
NWLG-NELG	E	35	35	35
NWLG-SWLG	E	4	4	4
NELG-SWLG	E	35	35	34
CNTR-NWLG	Z	12	12	12
CNTR-NELG	Z	17	17	17
CNTR-SWLG	Z	11	11	11
NWLG-NELG	Z	10	10	10
NWLG-SWLG	Z	2	2	2
NELG-SWLG	Z	10	10	10

Table 5.10: Differential RMS ground displacements, rounded up to the nearest nm, due to a 12-s noise spike produced by a medium-sized truck being driven along Langmuir Road on July 7, 2003. Most of the differential noise power due to the passing of the truck is in the 5-to-40-Hz range.

RMS ground displacement (nm)

Station component		Above 1 Hz	Above 2 Hz	Above 5 Hz
CNTR	N	3	3	2
NWLG	N	1	1	1
NELG	N	4	4	4
SWLG	N	2	1	1
CNTR	E	6	6	5
NWLG	E	2	1	1
NELG	E	4	3	3
SWLG	E	2	2	2
CNTR	Z	3	3	3
NWLG	Z	1	1	1
NELG	Z	2	2	2
SWLG	Z	2	1	1

Table 5.11: RMS ground displacements, rounded up to the nearest nm, due to a 150-kW generator run by a V12 Detroit Diesel engine for one hour, approximately 600 m from the center of the seismic array.

displacements that are not only within acceptable levels but also smaller (by a factor of at least 2) than the displacements typically caused by background seismic noise in the absence of transient phenomena during the noisiest nights of the year (subsections 5.1.1 and 5.1.2).

However, because it is unrealistic to picture telescope cooling systems with generators hundreds of meters away, the question that naturally arises is how close to the telescopes the generators can be without these making the ground shake too much. Although this can really only be answered by

Differential RMS ground displacement (nm)

Station component		Above 1 Hz	Above 2 Hz	Above 5 Hz
CNTR-NWLG	N	3	3	3
CNTR-NELG	N	4	4	4
CNTR-SWLG	N	3	3	3
NWLG-NELG	N	4	4	4
NWLG-SWLG	N	2	1	1
NELG-SWLG	N	4	4	4
CNTR-NWLG	E	6	6	6
CNTR-NELG	E	7	6	6
CNTR-SWLG	E	6	6	6
NWLG-NELG	E	4	4	3
NWLG-SWLG	E	3	2	2
NELG-SWLG	E	4	4	3
CNTR-NWLG	Z	3	3	3
CNTR-NELG	Z	4	4	4
CNTR-SWLG	Z	3	3	3
NWLG-NELG	Z	2	2	2
NWLG-SWLG	Z	2	1	1
NELG-SWLG	Z	2	2	2

Table 5.12: Differential RMS ground displacements, rounded up to the nearest nm, due to a 150-kW generator run by a V12 Detroit Diesel engine for one hour, approximately 600 m from the center of the seismic array.

performing the experiment of placing generators closer to the seismic stations (unfortunately no longer in place), if we consider one of the things we learned about vehicle engines in the previous subsection (namely, that wave amplitude grows exponentially rather than uniformly as a truck moves closer to a seismic station), then we can make the rather optimistic estimate that if the generator studied had been moved 50% closer to the center of the array, then perhaps the maximum differential ground displacement observed would have been 400% larger, namely some 24 nm, which is barely within acceptable levels. In other words, the optimistic estimate assumes that a decrease in separation by a factor of 2 could result in an increase of motion by a factor of perhaps only 2^2.

In any case, because the adequate installation of machinery at MRO is crucial for the correct operation of the interferometer, and because relocating machinery or circumventing issues related to its shaking the ground too much could be very costly and take months to complete after problems are spotted, it is highly recommended that the suitability of generator locations be tested by running the interferometer (in several of its configurations) with the generators operating in *preliminary* locations from which they can be moved if the performance of the interferometer is below satisfactory. (Needless to say, we have assumed that the generators to be installed at MRO will have roughly similar characteristics to the one investigated herein.)

CHAPTER 6

SUMMARY AND CONCLUSIONS

Seismic background noise exempt of transients and between 1 and 50 Hz is highly unlikely to cause problems to interferometry at the MRO site. Ground displacements produced by ambient seismic noise during the noisiest nights of the 36-week study period have been measured to be typically well below the upper bound for acceptable ground motion (25 nm), namely 7 to 8 nm on average, with a probability of only 15% that ground displacements will exceed 14 nm on any of the noisiest nights of the year, even during the periods of most pronounced wind activity. More importantly, measurements of differential ground displacements also remain well within the acceptable upper bound during the noisiest nights of the eight-month study period, namely 9 to 10 nm on average, with a probability of only 18% that differential ground displacements will exceed 15 nm on any of the noisiest nights of the year, even during the periods of most pronounced wind activity. Although vertical differential ground displacements could be, under the drastic and unlikely assumption of coherent motion exactly out of phase, as large as 36 nm if subject to the strongest wind speeds recorded ($\sim$18 m/s), motion between stations is generally incoherent (except within the oceanic microseism band, between about 0.1 and 0.7 Hz). Although we have found wind-to-ground coupling through trees not to be an effective source of seismic noise at the site, the building of MRO structures

may increase the effectiveness of this coupling.

While much of the emphasis of this study is on maximum rather than median or low noise periods at the site, the PSD plots and ground displacement tables for the median and lowest noise hours of each week in the study period (Appendices B and C) show that, in the absence of transient phenomena, nighttime noise levels at the site (> 1 Hz) typically reside close to the GSN low noise model and exhibit ground displacements that are most favorable for the operation of the interferometer.

Among the naturally-occurring transient phenomena capable of causing loss of interferometer coherence over 1-hour periods, are local earthquakes, moderately strong regional events, and strong long-distance earthquakes. Of these, small local earthquakes ($M_d < 2.0$) are the most frequently-occurring, but have durations so short that they only bias the typical ground displacement over 1-hour periods when they come in swarms of three or more. Such swarms were observed to cause near-to-unacceptable ground displacement on only two occasions during the entire 36-week period studied. Moderately strong regional earthquakes, such as those occurring at the Pacific-North American transform boundary, are also capable of inducing loss of interferometer coherence but are rare occurrences. Only one such earthquake was observed to cause unacceptable ground displacement at MRO during the study period. Strong long-distance earthquakes occur at most a few times a year and must have an epicenter relatively close to MRO for the seismic energy reaching the site to be strong enough to disturb the average hourly ground displacements. It has been estimated that the total operational downtime of the interferometer due

to earthquakes will be, at most, 21 hours a year: 3 due to local earthquake swarms, 10 due to regional earthquakes, and 8 due to teleseisms. Although high-amplitude, short-period peaks in ground motion related to local earthquakes that do not come in swarms were most probably undetected by the 1-hour-long displacement averages used in this study, it has been estimated from a 37-year-long record of local earthquake activity that at most 15 local earthquakes unrelated to swarms will compromise the operation of the interferometer on any particular year. Moreover, while any one swarm of small local earthquakes is capable of compromising operations for up to one hour or so, independent local earthquakes will compromise operations for no longer than a few minutes each time.

Traffic is the artificial transient phenomenon most likely to produce differential ground displacements (> 1 Hz) larger than 25 nm and thus induce loss of interferometer coherence. Nevertheless, establishing proper traffic regulations at and in the neighborhood of the MRO site should help circumvent this issue. We recommend that the parking lot at MRO be built as far away from the interferometer as possible and that astronomers move about the interferometer site in much lighter vehicles such as golf carts. Although the effect of machinery operating approximately 600 m away from MRO was deemed to be negligible for interferometry, machinery operating closer to the site (*e.g.*, power generators, cooling systems, etc.) will evidently have a more prominent effect. We strongly recommend that power generators not be installed permanently at MRO until the interferometer has been tested in several of its configurations with power generators running in preliminary locations from which they can be moved if interferometer performance is below satisfactory.

We conclude that the MRO site is moderate in seismic background noise for a continental interior site and is overall suitable for building and operating the proposed interferometer, should the issues above mentioned be given the appropriate consideration.

APPENDIX A

Rationale and recommendations for establishing a permanent broadband station at MRO

It could be greatly advantageous for astronomers at MRO to have a permanent broadband station at the observatory because, firstly, whenever the lock on the fringe pattern is lost for unknown reasons they will be able to take a look at a digital seismogram and determine whether the interruption was caused by an earthquake or other local ground motion. Moreover, astronomers will be able to assess how long they should wait before attempting to continue with their observations. For this matter, the Geophysics Department at New Mexico Tech would make available to MRO astronomers typical seismograms showing what local, regional, and long-distance earthquakes look like when they are recorded by the particular instrument that would be installed at MRO (in what follows we suggest one instrument in particular), as well as other transient phenomena of interest. For example, if one night the lock on the interference pattern is suddenly lost and the seismogram shows that a short (say, 30- to 60-s earthquake) just occurred, then the astronomer will know that a small-magnitude local earthquake was the cause of the disturbance and that, unless the earthquake is part of a swarm (see section 5.2.1), they can continue with their observations immediately. In the unlikely event that the earthquake was part of a swarm of earthquakes, the event would be followed by a series of similar earthquakes with, say, a half-hour interval between events (see

subsection 5.1.4), in which case astronomers may not wish to proceed with their observations until at least several minutes after the last earthquake. If, on the other hand, the seismogram showed not a local event but an earthquake with a much longer duration, then astronomers would be looking at either a regional or a long-distance earthquake, in which case they would be recommended to not continue with their observations until the earthquake signal blends in again with pre-earthquake background noise levels. This could take up to about one hour in the case of very large earthquakes. Even in the case of a loss of interferometer coherence during which the seismogram does not show an earthquake, having a local seismic record would definitely show that seismic ground motions are not the problem and that other instrumentation issues (*e.g.*, vibrations within the movable adaptive optics elements) need to be addressed.

We thus recommend that a Guralp CMG-3TD digital-output broadband seismometer be installed at MRO. Just like the STS-2/Quanterra seismic acquisition system used in this study (Chapter 3), the Guralp CMG-3TD has a flat velocity response between 120 s and 50 Hz as well as a 24-bit digitizer module. The seismometer package is offered in North America by Digital Technology Associates, Inc. (DTA) at U. S. $ 17,756.00 (quoted on January 20, 2004) and includes a GPS satellite receiver together with GPS cable and power data cable as well as a 64-MB flash RAM to store data in case the telemetry goes down temporarily (additional flash RAM can be obtained at U. S. $880.00 to bring the total RAM up to 512 MB). Personnel from the geophysics program at New Mexico Tech would be glad to assist and cost-share in the installation of the seismometer, which would be delivered by DTA 120 days upon request, as well as to service it when necessary. An Internet-connected PC running Guralp

software would be set up at MRO to facilitate data display and handling. DTA is located at 1330-A Galaxy Way, Concord, CA 94520 and can be reached by phone at (925) 682-2508 or by fax at (925) 682-2072.

APPENDIX B

Weekly Displacement PSD Plots

Displacement PSD plots for all characteristic 1-hour noise periods of each of the 36 weeks studies are included in the CD attached. Because a single PDF file with all 216 pages of color plots would be huge and therefore painful to handle in slow computers, the CD attached features twelve Appendix B PDF files. Each file contains the plots corresponding to three weeks according to the table overleaf. The legend for all plots is also shown. (Note: filenames may be displayed incorrectly in computers running Solaris 9 and older.)

The author is currently working on putting together *all* 1-hour-long PSD plots computed from the seismic data of each station component during the 36-week study period (i.e., *tens of thousands* of PSDs, not just the few PSDs corresponding to the characteristic noise hours of each week that go into this appendix) into a single plot which will in fact be a seismic noise probability density function for the station component in question. These probability density functions, which will in effect display all the seismic data acquired during this study, will be central to a short article summarizing this thesis that the MRO seismic characterization team plans to submit to an appropriate journal for publication in the near future.

File	Weeks
AppendixB1.pdf	7-9
AppendixB2.pdf	10-12
AppendixB3.pdf	13-15
AppendixB4.pdf	16-18
AppendixB5.pdf	19-21
AppendixB6.pdf	22-24
AppendixB7.pdf	25-27
AppendixB8.pdf	28-30
AppendixB9.pdf	31-33
AppendixB10.pdf	34-36
AppendixB11.pdf	37-39
AppendixB12.pdf	40-42

Noise curve	Color
CNTR	blue
NELG	magenta
NWLG	green
SWLG	cyan
GSN High	black (top)
GSN Low	black (bottom)

APPENDIX C

Weekly RMS Displacement Tables

RMS displacement tables for all characteristic 1-hour noise periods of each of the 36 weeks studies are included in the CD attached, which features six Appendix C PDF files. Each PDF file contains the tables corresponding to six of the weeks studied, as shown in the table below. (Note: filenames may be displayed incorrectly in computers running Solaris 9 and older.)

File	Weeks
AppendixC1.pdf	7-12
AppendixC2.pdf	13-18
AppendixC3.pdf	19-24
AppendixC4.pdf	25-30
AppendixC5.pdf	31-36
AppendixC6.pdf	37-42

APPENDIX D

Wind Statistics Table

Wind speeds and corresponding standard deviations are reported in m/s and are *median* speeds (expect where indicated by an asterisk, in which case a *mean* wind speed is reported) for the noisiest hour of each week studied. Wind directions and corresponding standard deviations are reported in degrees of azimuth, that is, degrees measured along the horizon and clockwise from north. A dash represents a standard deviation that was not calculated due to the our having just two data samples for that noisiest hour in question.

Week	Wind speed (m/s)	Std. dev. (m/s)	Wind direction °C	Std. dev. °C
7	18.2900	2.0773	246.4000	8.6709
8	13.0900	2.1687	330.0000	9.4444
9	13.4000	2.3665	235.8000	10.3385
10*	9.6000	-	292.5000	-
11*	6.3000	-	225.0000	-
12*	0.4000	-	315.0000	-
13	10.7800	1.4612	314.6000	13.2061
14	18.1800	2.6186	242.0000	8.2670
15	14.2800	2.7837	226.3000	16.3032
16	16.1600	3.0396	262.6000	11.9826
17	18.8000	2.4956	241.1000	10.5725
18	16.0000	2.3106	239.8000	10.2483
19	15.3200	1.8142	229.1000	13.5920
20	15.9200	2.5891	293.4000	11.0837
21	2.8130	2.1882	13.0000	72.4777
22	5.6450	2.2891	67.6600	19.8949
23	7.1200	1.5835	328.4000	16.4382
24	4.7730	0.6769	189.0000	11.9566
25	4.7530	0.9221	171.5000	17.1342
26	9.2250	2.5874	42.3700	11.3402
27	7.1200	1.2636	348.7000	19.9769
28	8.8700	1.8360	85.1000	12.8170
29	10.6700	2.9862	48.4800	10.9420
30	7.2500	1.6983	3.0360	17.8276
31*	7.8000	-	22.5000	-
32*	4.5000	-	33.8000	-
33*	2.5000	-	202.5000	-
34*	2.2000	-	157.5000	-
35	7.2000	3.8592	38.7300	18.7695
36	10.8100	1.2519	75.9000	9.8673
37	8.5000	1.1748	284.2000	8.8965
38	12.5700	1.4466	263.7000	8.2594
39	9.6400	1.5859	76.1000	10.4169
40	8.4700	1.6273	245.0000	11.7424
41	8.7500	1.6777	70.1000	10.3124
42	8.8000	1.3757	346.5000	18.6122

REFERENCES

Aki, K., and P. G. Richards (2002). *Quantitative Seismology*, University Science Books, Sausalito.

AMEC Earth & Environmental, Inc. (2004). Geotechnical engineering study report: Magdalena Ridge Observatory, South Baldy Peak, Socorro County, New Mexico. *AMEC Project No. 3-517-000123*, 119 pp.

Balch, R. S., H. E. Hartse, A. R. Sanford, and K. W. Lin (1997). A new map of the geographic extent of the Socorro mid-crustal magma body, *Bull. Seism. Soc. Am.* **87**, 174-182.

Bowring, S. A. (1980). The geology of the west-central Magdalena Mountains, Socorro County, New Mexico, *Master's Thesis*, New Mexico Institute of Mining and Technology, Socorro.

Bracewell, R. (1978). *The Fourier Transform and its Applications*, McGraw-Hill, New York.

Buscher, D. F., J. T. Armstrong, C. A. Hummel, A. Quirrenbach, D. Mozurkewich, K. J. Johnston, C. S. Denison, M. M. Colavita, and M. Shao (1995). Interferometric seeing measurements on Mt. Wilson: power spectra and outer scales, *Appl. Opt.* **34**, 1081-1096.

Chapin, C. E., and W. R. Seager (1975). Evolution of the Rio Grande rift in the Socorro and Las Cruces area, in *New Mexico Geol. Soc. Guidebook* **26**th Field Conf., 297-321.

Haniff, C. A., and D. F. Buscher (2003). Astronomical interferometry, *Physics World* **16**(5), 39-43.

Incorporated Research Institutions for Seismology Program for the Array Seismic Studies of the Continental Lithosphere (IRIS PASSCAL). "Strekeisen STS-2 response." <http://www.passcal.nmt.edu/instrumentation/Sensor/Response/sts2.html> (November 11, 2003).

Incorporated Research Institutions for Seismology (IRIS). "PASSCAL Field Manual." November 14, 1994. <http://www.iris.iris.edu/passcal/Manual> (March 27, 2004).

Lin, K.-W. (1999). Probabilistic seismic hazard for New Mexico and bordering areas, *Ph. D. Thesis*, New Mexico Institute of Mining and Technology, Socorro.

Peterson, J. (1993). Observations and modeling of seismic background noise. *U.S. Geol. Surv. Open-File Rept. 93-322*, 95 pp.

Sanford, A. R., K. W. Lin, I. C. Tsai, and L. H. Jaksha (2002). Earthquake catalogs for New Mexico and bordering areas: 1869-1998, Circular 210, New Mexico Bureau of Geology and Mineral Resources.

Sheriff, R. E. (1973). *Encyclopedic Dictionary of Exploration Geophysics*, Society of Exploration Geophysicists, Tulsa.

Stacy, A. L. (1968). Geology of the area around the Langmuir Laboratory, Magdalena Mountains, Socorro County, New Mexico, *Master's Thesis*, New Mexico Institute of Mining and Technology, Socorro.

Uhrhammer, R. A., and W. Karavas. "Guidelines for installing broadband seismic instrumentation." June 6, 1997. <http://www.seismo.berkeley.edu/seismo/bdsn/instrumentation/guidelines.html> (March 26, 2004).

Weber, R. H. (1963). Cenozoic volcanic rocks of Socorro County, in *New Mexico Geol. Soc. Guidebook* **14**th Field Conf., 132-143.

Welch, P. (1967). The use of Fast Fourier Transform for the estimation of power spectra: a method based on time averaging over short, modified periodograms, *IEEE Trans. Audio Electroacoustics* AU15, 70-73.

Wielandt, E. (2002). Seismic sensors and their calibration, in Bormann, P. (ed), *New Manual of Seismological Observatory Practice*, Volume 1, GeoForschungsZentrum, Potsdam.